UNIVERSITY OF OULU

DEGREE PROGRAMME IN WIRELESS COMMUNICATIONS ENGINEERING

MASTER'S THESIS

MAP-BASED CHANNEL MODEL PARAMETERIZATION AND COMPARISON OF THREE DIFFERENT DETERMINISTIC CHANNEL MODELLING METHODS

Author	Gowshigan Selvarasa
Supervisor	Dr. Markus Berg
Second Examinor	Dr. Pekka Pirinen
(Technical Supervisor)	Dr. Antti Roivainen

June 2019

Selvarasa G. (2019) Map-based channel model parameterization and comparison of three different deterministic channel modelling methods. University of Oulu, Degree Programme in Wireless Communication Engineering, 67 p.

ABSTRACT

The interest in studying the channel characteristics is exponentially increasing with the growth of the communication systems. Various channel modelling approaches have been discussed in the past decades. The ray tracing based channel models are distinguished from the other channel models as they considers the environmental information and thus are expected to reflect the real propagation phenomena that exist in that specific environment. The goal of this thesis is to study the propagation channel characteristics of the three different channel models. The two deterministic channel models are the simplified map-based ray tracing channel model implemented in the METIS project and the full ray tracing based channel model implemented by the Beijing Jiaotong University. The third channel model is the hybrid model based on METIS map-based channel. It uses the deterministic part of the METIS map-based channel model.

Full ray tracing based models require detailed description of the propagation environment or map and they target on site-specific channel modelling. Such site-specific models are not typically required in performance testing of devices, where the target is to ensure device performance in a typical propagation environment and possibly to cover some extreme cases. The simplifying map-based approach contradicts with the full ray tracing method in the way that the information of the map is reduced by approximating the building shapes and introducing artificial tiles to make scattering in the walls and ground reflections. Map-based channel modelling provides additional realism in channel models compared to traditional stochastic models applied in performance testing.

The urban street canyon scenario was chosen to be modelled. The comparison was carried out at 3.5 GHz by means of performance metrics such as total path loss, LOS and NLOS propagation conditions at UE positions, K-factor, RMS delay spread, statistics of angles, angle spreads, and cross polarization ratios.

The results have showed similarities in LOS UE positions and dissimilarities in NLOS UE positions. The reasons are identified and explained in the discussion section. It is decided to investigate the radio channel characteristics of METIS map-based channel model and hybrid channel model for the future study purpose.

Keywords: ray tracing, channel model, hybrid channel model, K-Factor, RMS angle spread, simplified map-based channel model.

TABLE OF CONTENTS

FOREWORD

This thesis is focused on studying on map-based channel model parameters and comparing three different deterministic channel models. This thesis was written during my internship at Keysight Technologies Finland Oy. I express my appreciation to the software team manager Jyrki Matero, and the internship supervisor Pertti Kangas for offering me an opportunity to work as an intern. I would like to thank my technical supervisor Dr. Antti Roivainen for his immense support and advises on my thesis. I would also thank Dr. Pekka Kyösti for his valuable teaching and comments on my work. In addition to that, my thanks also go to Jukka Kyrölainen who initially helped in preparing the thesis title and later provided me his insightful advices and discussions. My gratitude also goes to my university supervisor Dr. Markus Berg, who patiently helping me till the end of my thesis. I am grateful to the second examiner Dr. Pekka Pirinen, for his comments on my thesis and irreplaceable support in revising my work. Furthermore, I appreciate the help of Dr. Danping He and her assistant Luoyan Zho for providing the map and giving enough guidance to use their tool. In addition to that, I am obligated to thank all my Keysight colleagues who have shared their knowledge and motivated me throughout this thesis period.

LIST OF ABBREVIATIONS AND SYMBOLS

2G	Second Generation
3D	Three Dimensional
3GPP	Third Generation Partnership Project
5G	Fifth Generation
AOA	Azimuth Angle of Arrival
AOD	Azimuth Angle of Departure
ASA	Azimuth Spread of Arrival angle
ASD	Azimuth Spread of Departure angle
BS	Base Station
CAS	Circular Angle Spread
CDF	Cumulative Density Function
D2D	Device to Device
DR	Dynamic Range
DS	Delay Spread
EOA	Elevation Angle of Arrival
EOD	Elevation Angle of Departure
ESA	Elevation Spread of Arrival angle
ESD	Elevation Spread of Departure angle
FDTD	Finite Difference Time Domain Method
FULLRT	Full Ray Tracing
GCS	Global Coordinate Systems
GO	Geometric Optics
GSCM	Geometric Based Stochastic Channel Model
GTD	Geometry Theory of Diffraction
HH	Horizontal to Horizontal
HV	Horizontal to Vertical
KF	K-Factor
IO	Interaction Object
LCS	Local Coordinate System
LOS	Line of Sight
METIS	Mobile and wireless communications Enablers for the Twenty-twenty Information Society
mmWave	MilliMeter Wave
MOM	Method of Moments
MPC	Multi-Path Component
NLOS	Non Line Of Sight
O2I	Outdoor to Indoor
O2O	Outdoor to Outdoor
PAS	Power Angular Spectrum
PDF	Probability Density Function
Rx	Receiver
RMS	Root Mean Square
RT	Ray Tracing
SD	Standard Deviation
Tx	Transmitter

UE	User Equipment
UMa	Urban Macro
UMi	Urban Micro
V2V	Vehicle to Vehicle
VH	Vertical to Horizontal
VV	Vertical to Vertical

A	Propagation Matrices or Polarization Matrices
AR	Angle Range
AS	Angle Spread
D	Angle width defined for either azimuth or elevation
d	Distance to first/last interaction point from Tx/Rx
d_0	Reference distance
d_a	Space between antenna elements
$d_{rx,u}$	Location of the u^{th} element of the receiver antenna
$d_{tx,s}$	Location of the s^{th} element of the transmitter antenna
E	Electric field
F	Divergence Factor
f	Frequency
$F_{rx,u,\theta}$	Field pattern of the receive antenna from u^{th} element in the direction of θ
$F_{rx,u,\phi}$	Field pattern of the receive antenna from u^{th} element in the direction of ϕ
$F_{tx,s,\theta}$	Field pattern of the transmit antenna from s^{th} element in the direction of θ
$F_{tx,s,\phi}$	Field pattern of the transmit antenna from s^{th} element in the direction of ϕ
G^{rx}	Gain of the receiver
G^{sc}	Scattering gain
G^{tx}	Gain of the transmitter
G_u^{rx}	Gain of the receiver from u^{th} element
G_s^{tx}	Gain of the transmitter from s^{th} element
h	Channel impulse response
$H_{u,s}$	Channel impulse response to u^{th} receive antenna element from s^{th}transmit antenna elemant
$K_{n,m}$	Cross-polarization ratio of the n^{th} sub-path the m^{th} path
L	Loss
$n1$	Refraction index of medium 1
$n2$	Refraction index of medium 2
$P_{n,m}$	Power of the n^{th} sub-path the m^{th} path
P_m	Power of the m^{th} path
P_{rx}	Received power
P_{tx}	Transmitted power
R_{rx}	Location of the receiver
R_{tx}	Location of the transmitter
S_D	Distance to UE from the diffraction point

S_{in}	Distance to BS from the diffraction point
S_s	Distance between the receiver node and the scattered node
T	Transpose operation
v	Doppler shift
v_f	Fresnel parameter
w_k^D	Doppler frequency
α_m	Offset angle
α_t	Steering Vector
α_{vv}	Received amplitude of the vertically polarized antenna in vertical polarization direction
α_{vh}	Received amplitude of the vertically polarized antenna in horizontal polarization direction
α_{hv}	Received amplitude of the horizontally polarized antenna in vertical polarization direction
α_{hh}	Received amplitude of the horizontally polarized antenna in horizontal polarization direction
$\alpha_{\theta\theta}$	Electric field of the ray arrive with angle θ and departure with angle θ
$\alpha_{\theta\phi}$	Electric field of the ray arrive with angle θ and departure with angle ϕ
$\alpha_{\phi\theta}$	Electric field of the ray arrive with angle ϕ and departure with angle θ
$\alpha_{\phi\phi}$	Electric field of the ray arrive with angle ϕ and departure with angle ϕ
ϵ_1	Relative permittivity of medium 1
ϵ_1	Relative permittivity of medium 2
θ	Angle
θ_i	Incident angle
θ_t	Transmitted angle
θ_r	Reflected angle
$\theta_{n,m,u}$	Mean angle
τ	Delay
τ_0	Mean delay
τ_l	Delay of the l^{th} path
τ_m	Delay of the m^{th} path
ρ_{TE}	Reflection coefficient of TE wave
ρ_{TE}	Transmission coefficient of TE wave
Ω	AOD
Ψ	AOA
$\cdot$	Scalar Product
$\dagger$	Transpose Operation

1 INTRODUCTION

The essential parts of communication systems are the transmitters, the channels, and the receivers. The knowledge about the variation of channel characteristics and the critical values of channel characteristics is paramount to design communication system and performance testing of communication devices. Therefore, it is essential to know a reliable channel model to design a system that works well in the real environment. The signal transmitted from a transmitter undergoes various changes due to reflection, absorption, attenuation, dispersion, refraction, and diffraction. These phenomena modify the signal in many ways, attenuation causes amplitude change, dispersion in delay spreads the signal in the time domain, refraction due to various mediums bends the signal and diffraction by the edges of an object cause scattering. Therefore, it is critical to know how these phenomena affects channel response.

When 2G systems were in use, the path loss model was fairly enough to design the system. But the growth of generations from 2G to 5G and beyond has made it more challenging to design a system by requiring high accuracy while increasing the system complexity.

The devices used in 5G and beyond are expected to work in the frequency range 500 MHz to 1 THz [1]. In addition to that, it is expected that 5G will facilitate different use cases such as high-speed broadband, machine-to-machine, device-to-device, vehicle-to-vehicle and high-speed train communications. In order to facilitate these, it is required to have a data rate of 10 Gbps, cell edge rate grater than 100 Mpbs and latency less than 1 sec [2]. The new scenarios of interests have be identified in [3], such as Urban Micro (UMi) with Outdoor to Outdoor (O2O) and Outdoor to Indoor (O2I), Urban Macro (UMa) with Outdoor to Outdoor (O2O) and Outdoor to Indoor (O2I), indoor, backhaul and device to device/ vehicle to vehicle (D2D/V2V).

These advance requirements have demanded the additional requirements for new channel models. To address these demands, various proposals are found in the literature. Such proposals are, extending the existing 3D channel model in 3GPP (3GPP 3D), supplementing the additional requirements of 5G, increasing the supported frequency to up to 100 GHz, supporting the channel bandwidth in the range 100 MHz to 2 GHz, accommodating the mobility scenarios D2D and V2V, hence expected to support the UE speed up to 500 km/hr [2]. In addition to that, consideration of spatial consistency, support of the range of antenna arrays such as linear, planar, cylindrical, and spherical arrays with arbitrary polarization, temporal and frequency consistency, less computation complexity and higher accuracy, consideration of propagation condition, modelling of polarization characteristics, backward compatibility, and blockage modelling are suggested in [4]. Moreover, the author in [5] has addressed the requirement of new modulation waveforms.

Map-based modelling utilizes ray tracing to find the paths. Since it uses the environmental information in the form of digital information, it is expected to replicate the propagation phenomena exists in the real environment. In addition to that, it follows the deterministic approach and includes the propagation mechanisms such as penetration, diffraction, specular reflection, and diffuse scattering, penetration. The channel impulse response of each path provides the information distance, incident angle, reflected/diffracted/scattered angle as well as the electromagnetic property of the corresponding material. Therefore, the spatial and temporal consistency is guaranteed [6].

Moreover, the ray tracing methods are proven to give more accuracy as they are site-specific and the properties of each ray discovered via ray tracing provides the knowledge about the path loss, propagation delay, angle of arrival and angle of departure.

Even though map-based channel modelling provides all these benefits, challenge appears as the complexity increases when the map size increases and it requires enormous computation power and time. The author in [7], describes how adding a stochastic part on top deterministic part will reduce complexity and give more realism.

In channel modelling, it is often interesting to know the variation of channel characteristics in the domains such as path loss, time, delay, doppler shift, and polarization. The critical values are often required by the designers to design the system to perform at various extreme scenarios. In this thesis, it is aimed to compare the three channel models: two models with the same modelling principles but using the simplified map with METIS map-based model and other model is a hybrid model. The full ray tracing based channel model is developed by the Beijing Jiatong University. The METIS map-based model has been developed in the METIS project. The hybrid model has been developed by Keysight Technologies Oy.

1.1 Overview of thesis

This thesis is focused on comparing two deterministic channel models and one hybrid model. The thesis is structured as follows: In Chapter 1, the radio channel and the importance of channel modelling from 2G to 5G and beyond is introduced. Subsequent chapters describe the background theories for channel modelling and depict the ray-tracing and hybrid-based channel modelling approaches and channel modelling comparison parameters. In Chapter 2, the radio channel is introduced, the propagation mechanisms are elaborated and the description of the channel is presented. Chapter 3, discusses the simplified map-based ray tracing, the hybrid channel modelling methods and the channel modelling tools used are briefly described. Chapter 4 brief the comparison metrics and elaborate the application of them in comparing the channel models. Chapter 5 includes the simulation settings and the comparison results. Later subjects Chapter 6 and 7 present the discussion and conclusion of the findings in this thesis.

2 WAVE PROPAGATION AND RADIO CHANNEL

In this chapter, the basic concepts and literature related channel modelling are discussed. At first, the propagation mechanism is introduced and later the channel modelling descriptions, modelling methods, and fundamental theories associated with them are presented. The channel modelling aims to mathematically describe the behavior of the channel. The following propagation mechanisms are found in literature: the free space propagation, reflection, refraction, absorption, scattering, and diffraction [8]. Next, we discuss about the propagation phenomena briefly.

2.1 Propagation mechanism

Radio propagation is influenced by the propagation phenomena, which are illustrated in Figure 1.

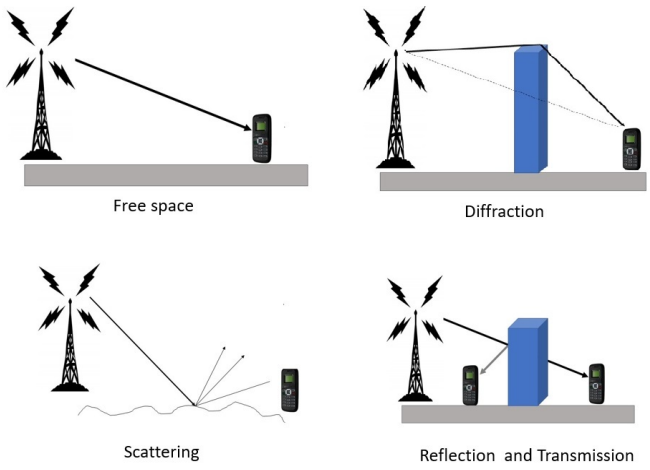

Figure 1. Main propagation phenomena.

The amplitude and the phase of ray is changed by these phenomena. Therefore, it is essential to study the physical and mathematical description of the fields and the phase change of the ray that experiences these phenomena.

2.1.1 Line of sight propagation

Path loss is the loss the signal experiences by traveling by far distances. Path loss models for various propagation scenarios are proposed in [9]. For a line of sight propagation, the received power from a transmitter separated by distance d can be given by well-known Friis' free space path loss law as [10]

$$P_{rx}|_{dBm} = P_{tx}|_{dBm} + G_{tx}|_{dB} + G_{rx}|_{dB} + 20\log(\frac{\lambda}{4\pi d_0}) - 20log(\frac{d}{d_0}), \qquad (1)$$

where d_0 is an arbitrary reference distance and often considered as equal to 1, d is the distance of the receiver from the transmitter, G_{tx} is the gain of the transmitter antenna, G_{rx} is the gain of the receiver antenna, P_{rx} is the received power, P_{tx} is the transmitter power and λ is the wavelength. The corresponding path loss PL can be calculated by

$$PL[dB] = P_{tx}[dB] - P_{rx}[dB] + G_{tx}[dBi] + G_{rx}[dBi] - L[dB] = 20\text{lg}(4\pi d) - 20\text{lg}(\lambda), \tag{2}$$

where P_{rx}, P_{tx} are the received and transmitted powers. The author in [1] has categorized the various path loss models based on their applicability. In free space path loss calculation, the effect of the antennas on both the transmitter and the receiver are not taken into account and the isotropic propagation is considered.

2.1.2 Reflection and refraction

The reflection or specular reflection is distinguished from diffuse reflection by the situation where the incident angle is equal to the reflected angle. In ray tracing, the interest is to know the change of the direction of the ray and the amplitude of the incident, reflected, and transmitted ray. Figure 2 depicts the reflection and refraction mechanism.

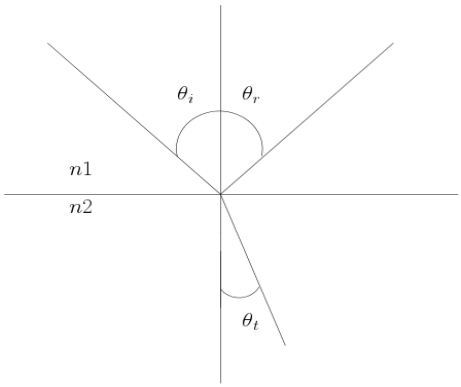

Figure 2. Reflection and refraction between two medium distinguished by different refraction indices. The angles θ_i, θ_t, θ_r are incident, transmitted and reflected angles.

The reflected and refracted angle can be calculated with respect to incident angle. The transmitted and the reflected ray that has traversed from the first medium to the second medium is governed by the well-known Snell's law, and the relation between angles θ_i and θ_t is shown in [8] as

$$\frac{sin\theta_i}{sin\theta_t} = \frac{n1}{n2}, \tag{3}$$

where $n1$ and $n2$ are the refraction indices of the ray impinging and refracting medium. The amplitude of the reflected and transmitted ray is calculated relative to the incident wave amplitude by the Fresnel reflection and transmission coefficients. Given that the ϵ_1 and ϵ_2 are the dielectric constants of the two materials, the Fresnel transmission and reflection coefficients in the cases where the electric field vector is parallel to the interface of two dielectrics (transversal electric wave, TE wave) and the case where the magnetic field is parallel to the interface(transversal magnetic field,TM wave) can be

calculated as follows. The reflection and the transmission coefficients of the TE wave are given as [10]

$$\begin{aligned} \rho_{TE} &= \frac{\sqrt{\epsilon_1}cos(\theta_i) - \sqrt{\epsilon_2}cos(\theta_t)}{\sqrt{\epsilon_1}cos(\theta_i) + \sqrt{\epsilon_2}cos(\theta_t)} \\ T_{TE} &= \frac{2\sqrt{\epsilon_1}cos(\theta_i)}{\sqrt{\epsilon_1}cos(\theta_e) + \sqrt{\epsilon_2}cos(\theta_t)}. \end{aligned} \tag{4}$$

Similarly the reflection and the transmission coefficients of the TM wave can be given as

$$\begin{aligned} \rho_{TM} &= \frac{\sqrt{\epsilon_2}cos(\theta_i) - \sqrt{\epsilon_1}cos(\theta_t)}{\sqrt{\epsilon_2}cos(\theta_i) + \sqrt{\epsilon_1}cos(\theta_t)} \\ T_{TM} &= \frac{2\sqrt{\epsilon_1}cos(\theta_i)}{\sqrt{\epsilon_2}cos(\theta_i) + \sqrt{\epsilon_1}cos(\theta_t)}. \end{aligned} \tag{5}$$

2.1.3 Diffraction

Pioneering work on diffraction was carried out by Keller[11] with the introduction of geometrical theory of diffraction (GTD) by Keeler. The electric field of a diffracted ray is given by [10]

$$E_{total} = exp(-jk_o x)(\frac{1}{2} - \frac{exp(j\pi/4)}{\sqrt{2}}F(v_F)), \tag{6}$$

$$F(v_F) = \int_0^{v_F} exp(-j\pi\frac{t^2}{2})dt, \tag{7}$$

where k_0, λ, $F(v_F)$, v_F represent the wave-number, wavelength, Fresnel integral, and Fresnel parameter, respectively. There is alternative approach to calculate the loss due to diffraction, which is proposed by Jan-Erik Berg [12]. This original method is to calculate the path loss for micro-cell in the environment where surrounding buildings heights are larger than the antenna's height. However, this is used in calculating the loss from a diffraction point considering it as a secondary transmitting source.

2.1.4 Scattering

Reflection or specular reflection happens if the incident medium is smooth but if the incident medium is rough then the ray is scattered in multiple directions. There are several methodologies found in the literature to model the scattered rays. The well-known Lambertian based method models the scattered rays by considering the scattering source as a transmitter. But one of the downsides of this method is that the influence of polarization is not considered. This method was further developed by the [13] with the ability to tune the main parameters and extensions of this model to support the ultra-wideband signal was carried out by [14].

2.2 Multipath propagation

In this section, we introduce the multipath propagation and its effect in the propagation environment. The multiple replicas of the signal reach the receiver via multiple paths with each rays having different delay, phase, angle of arrival, angle of departure, and attenuation. These effect are caused by the different propagation mechanisms explained in Section 2.1.

1. Fading: the amplitude variation caused by the superposition of MPC.
2. Frequency dispersion: caused by the movement of the transmitter or the receiver or the interacting objects.
3. Delay dispersion: delay is the time taken to the signal to travel through a specific multipath component.
4. Polarization dispersion: reflection or diffraction causes changes in polarization state thus making it necessary to consider polarization changes from the transmitter to the receiver.

Therefore, it is essential to consider the multipath propagation and characteristics of mutlipaths such as reflection, transmission, and diffraction.

2.3 Deterministic channel description

From legacy systems to 5G and beyond the mathematical description of the channel has evolved representing information from various domains such as time, spatial, and polarimetric. This section briefly discusses the mathematical descriptions that used to describe channel response based on the requirements.

The impulse response the of channel is often described as a mathematical expression. In legacy systems, the impulse response of SISO channel is calculated by [10]

$$h(t,\tau) = \sum_{i=1}^{L} a_i(t)\delta(\tau - \tau_i), \tag{8}$$

where a_i is the complex amplitude of the i^{th} MPC and τ_i is the multipath delay. It can be observed that the channel response is a sum of each multipath component response. This can be further extended to the MIMO system as

$$\begin{aligned} h(t, r_{tx}, r_{rx}, \tau, \Omega, \Psi) &= \sum_{l=1}^{L} h_l(t, r_{tx}, r_{rx}, \tau, \Omega, \Psi) \\ &= \sum_{l=1}^{L} a_l \delta(\tau - \tau_l)\delta(\Omega - \Omega_l)\delta(\Psi - \Psi_l), \end{aligned} \tag{9}$$

where R_{tx} and R_{rx} are the coordinates of the receiver and transmitter antenna, Ω is the azimuth angle of departure (AOD) and Ψ is the azimuth angle of arrival (AOA). The

equation (9) includes the complex gain of the multipath components and the receiver and transmitter gains are not considered. Therefore, MIMO systems with the antenna types other than isotropic this can be extended as

$$\begin{aligned} h_{i,j} &= h(r_{tx}^{(j)}, r_{rx}^{(j)}) \\ &= \sum_{l} h_l(r_{tx}^{(1)}, r_{rx}^{(1)}, \tau, \Omega_l, \psi_l)\tilde{G_{tx}}(\Omega_l)\tilde{G_{rx}}(\Psi_l)\delta(\tau - \tau_l) \\ & exp(jk(\Omega_l) \cdot (r_{rx}^{(j)} \cdot r_{rx}^{(1)}))exp(jk(\psi_l) \cdot (r_{rx}^{(i)} \cdot r_{rx}^{(1)})), \end{aligned} \tag{10}$$

where the symbol "$\cdot$" denotes the scalar product. The equation (10) calculates the gain in the direction of Ω_l. Therefore, it is necessary to know the steering vector α_{tx}. For the transmit and receive antennas with the spacing d_a, the TX steering vector can be defined as:

$$\alpha_{tx}(\Omega) = \frac{1}{\sqrt{N_{tx}}}[1, exp(-j2\pi\frac{d_a}{\lambda}sin(\Omega)) \dots exp(-j2\pi(N_{tx}-1)\frac{d_a}{\lambda}sin(\Omega))]^T. \tag{11}$$

The steering vector of the receiver antenna is also defined in the similar fashion. The corresponding impulse response can be computed as

$$H = \int\int h(\tau, \Omega, \Psi)\widetilde{G}_{tx}(\Omega)\widetilde{G}_{rx}(\Psi)\alpha_{rx}(\Psi)\alpha_{tx}^{\dagger}(\Omega)d\Psi d\Omega, \tag{12}$$

where "†" denotes the transpose operation. If the dual polarized antennas are deployed, the polarization of the antenna needs to be considered. The dual polarized antennas are capable of transmitting both horizontal and vertical waves V and H, respectively. For antenna systems with polarized components the channel model characterization follows as

$$h(t, r_{tx}, r_{rx}, \tau, \Omega, \psi) = \sum_{l=1}^{L} \left(\begin{bmatrix} \alpha_l^{vv} & \alpha_l^{vh} \\ \alpha_l^{hv} & \alpha_l^{hh} \end{bmatrix} \right) \delta(\tau - \tau_l)\delta(\Omega - \Omega_l)\delta(\Psi - \Psi_l), \tag{13}$$

where, α is the amplitude from vertically polarized transmitter antenna to vertically polarized receiver antenna. The symbols vv, vh, hv, and hh represent the corresponding polarization configuration of the antenna.

3 CHANNEL MODELLING METHODS

The channel modelling methods are divided into two; stochastic based modelling and deterministic channel modelling. Such channel modelling methods are further categorized in Figure 3. The purpose of the channel modelling is to drive a mathematical description of behavior of the channel so that the behavior of channel in the domains such as path loss, time, delay, doppler, spatial, and polarimetric can be studied. The stochastic based methods generate fading coefficients based on a stochastic distribution. These distributions are derived by doing large measurement campaigns. Deterministic modelling tries to reproduce the actual links existing in the typical environment by considering the environmental information such as geometry of the building, terrain, etc.

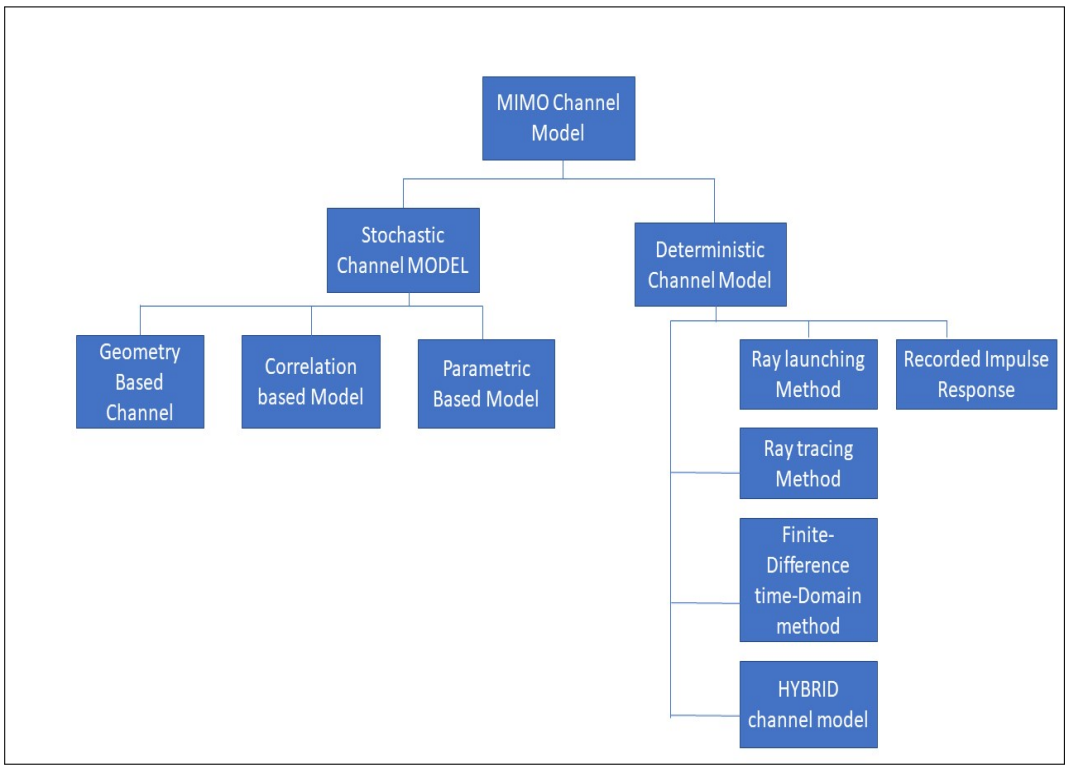

Figure 3. Channel modelling methods.

In this thesis, three channel models are used to compare the channel characteristics. METIS map-based model and full ray-tracing based model (FULLRT) are based on the deterministic modelling methods. The hybrid model is developed by combining the advantages of deterministic and stochastic methods.

3.1 Deterministic channel modelling

The deterministic method is the method, which uses digital maps or the geographical information about the specific place. The information can be geometry of the buildings, architectural types, material information about the buildings, scattering object (people, vehicles), and weather condition, etc. The deterministic channel models

are also called as site-specific channel models as they replicate the links specific to a particular environment and thus those channel models cannot be applied in any other environments.

One of the commonly used deterministic channel models is the ray tracing based channel model. Full ray tracing methods yield precise modelling of the propagation channel characteristics of the modelled environment. Thus, it provides the accurate data of the discovered rays. Such parameters are 3D distance, time, delay, and field strength at the receiver, and angles of arrival and departure. However, this requires an accurate map of the environment. The environment changes time to time and it often requires updates to data bases. One of the challenges in the RT based method is finding an updated map. RT based channel models are required by wireless service operators to optimize their base stations in specific environments. However, in performance testing it is not necessary to have such site-specific channel models. These map-based channel models have proved to provide additional realism over stochastic methods. The simplified map-based channel model was developed in the METIS project. That model is also based on ray tracing [15]. The underlying idea of hybrid modelling is that, it combines the advantage of deterministic modelling and stochastic modelling. It utilizes the radio environment and the information about propagation condition from deterministic modelling. Stochastic method is applied to model the effects that cannot be described by the map [16].

3.1.1 Ray tracing based channel modelling

The ray is conceptualized as a line starting from one point and go towards the infinity. One paradigm for a ray is the light originated from a source, such as sunlight. The ray has properties such as position, direction, amplitude, phase, and polarization [17]. The ray tracing method (RT) is considered as a superior method due to the following advantages. It is site-specific, claimed to provide high accuracy with MIMO systems, and offer accurate space-time results. In addition to that, this method provides an effective way to visualize the interaction of EM waves and it is said to be independent of the bandwidth and the carrier frequency [18, 19]. The study in [20] shows that the capacity rate calculation for the urban microcells is more informative than the conventional approach. This RT based channel modelling requires the description of an environment with the information of building walls and other elements of building such as windows and roof, bridges, terrain information, trees, etc. The goal of the ray tracing based channel modelling is to model the real links in the propagation environment. It is carried out by tracing the path of the ray that embarks from the transmitter and reaches the receiver. The types of rays includes LOS, reflected, diffracted, scattered and penetrated rays. One of the methods to trace the ray is based on the image based or backwards ray tracing, which is illustrated in Figure 4.

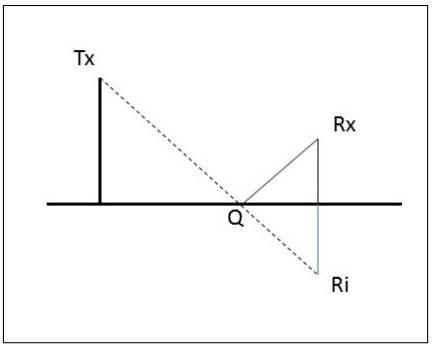

Figure 4. The image based method.

If the Tx and Rx locations and heights are known then the imaginary line to Ri can be drawn. The line which connects the Tx and Ri gives the reflecting point at earth or any surface. Now the path of the ray is determined. This is the first order reflection. This simple approach can be followed to calculate multiple reflections. A tree is drawn by considering each images identified through this method. An image is considered as one path segment. Several path segments together construct a ray. If one or more images is saved then it is considered as a valid ray. It is also possible to model a penetrated ray by considering the internal reflection and refraction. The reflected and refracted angles are governed by the Snell's law. The scattered rays are modelled as considering the scattering source as a secondary transmission source. In practice, a ray contains multiple interactions combined together.

In ray tracing approach channel transfer function can be composed as [19].

$$H_i(f) = a_i(f)e^{i\psi(f)} \tag{14}$$

$$= \delta(\theta_{AOD} - \theta_{AOD,i})\delta(\theta_{EOD} - \theta_{EOD,i})\delta(\theta_{AOA} - \theta_{AOA,i})\delta(\theta_{EOA} - \theta_{EOA,i}) \tag{15}$$

$$H(f) = \sum_{i=1}^{Nrays} G'_{tx} H_i(f) G_{rx} \tag{16}$$

where the parameters AOA, AOD, EOA, EOD, delay, the electric field at the receiver point, and the path length need to be known. The complexity of ray tracing grows exponentially with increasing deterministic information.

3.1.2 METIS map-based channel modelling tool

The implementation of the METIS map-based modelling tool requires wall coordinates of a building, coordinates of the antenna and the receiver, in the global coordinate system as an input. The map is simplified in order to use it with the current implementation of METIS map-based model. Simplifying reduces the number of the building by considering the necessary buildings and shaping the buildings to be as rectangular or square faced. In addition to that all buildings which have more than four faces or irregular shape are reduced to four shaped rectangular or square faced buildings.

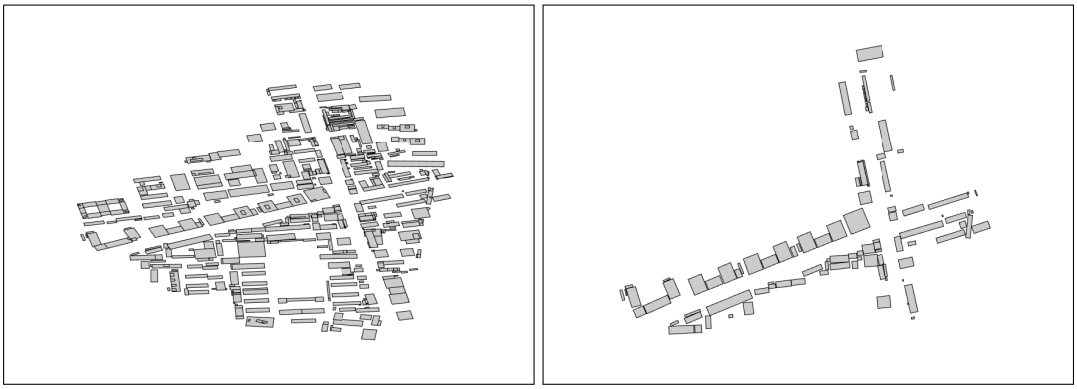

(a) (b)

Figure 5. The picture shows the original and the simplified map : (a) Map after conversion from sketch file, (b) Map after simplification.

Figure 5 illustrates the original map and the simplified map. The transmitter or Tx point is considered as the first node and the algorithm searches for the second node by searching the walls that are LOS or via specular reflection. This search procedure discovers the possible building for the next interaction.

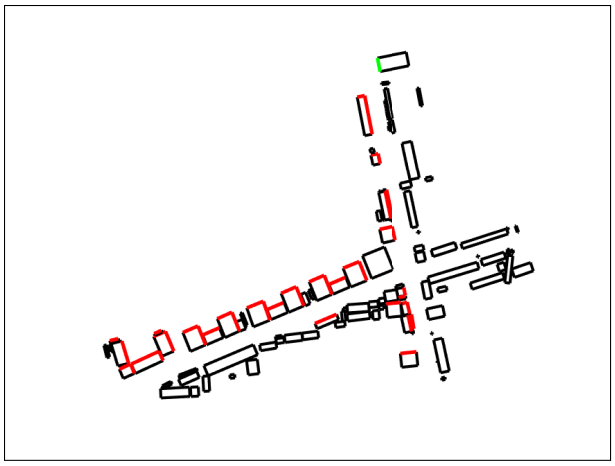

Figure 6. LOS walls.

Figure 6 shows examples of this LOS wall searching procedure. The walls that are LOS to the green colour wall are highlighted by the red colour. The possible second nodes can be interaction points such as reflecting, scattering, diffuse scattering objects or sources are searched. It is carried out by searching the walls, which are visible to the MS and the BS. It is illustrated in Figures 7 and 8.

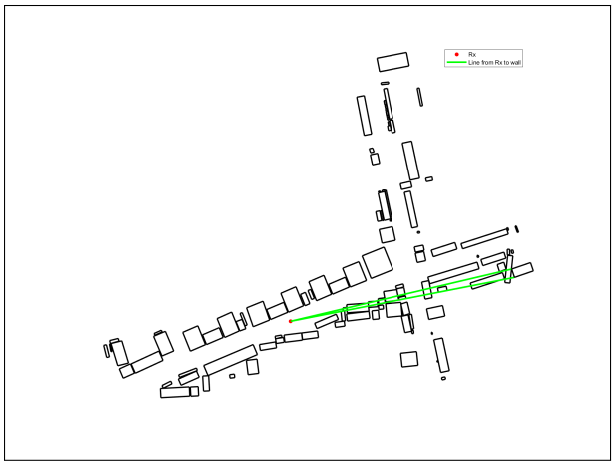

Figure 7. LOS walls to MS.

Figure 7 illustrates the possible direct paths from the UE to a wall. This procedure assists in finding the possible path to a receiver after an interaction. Similarly, the walls, which are not blocked by any object or buildings are identified by Tx to LOS checking, which is presented in Figure 8.

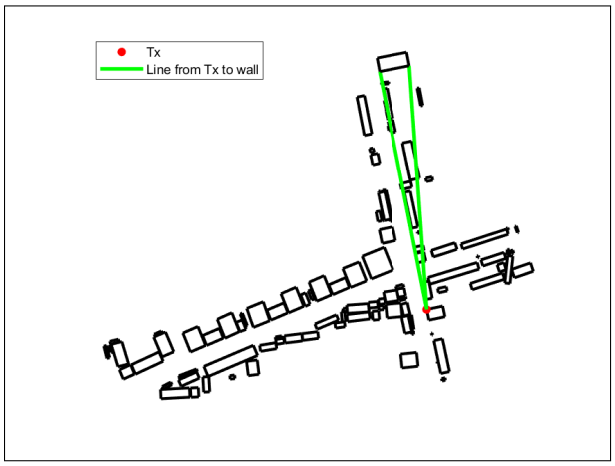

Figure 8. LOS walls to BS.

The METIS implementation supports the rays that are combined with the multiple propagation mechanism and which are presented below. It supports reflection of order 2 and it is possible to have three interaction in one path. However, the current implementation does not consider penetration.

Therefore, the typical ray will have multiple interactions as shown in Figure 9.

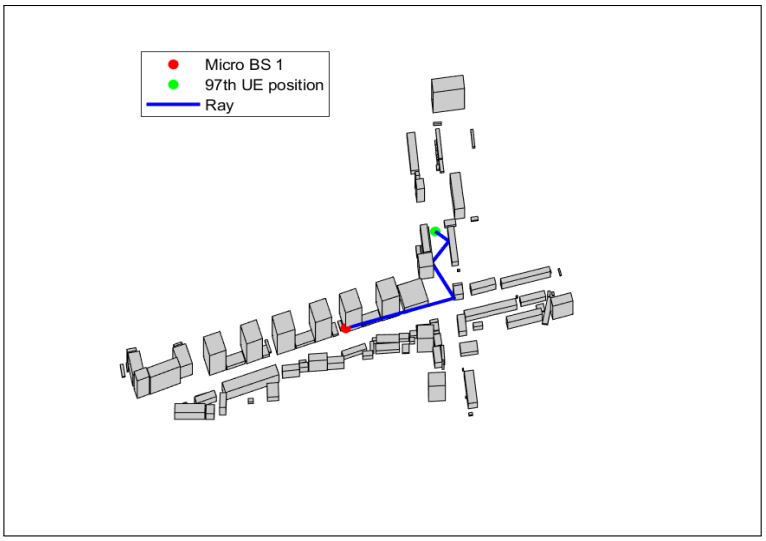

Figure 9. Illustration of the actual path found for one Tx and Rx position.

Figure 9 illustrates the typical path found for one UE position and a micro base station. The corresponding ray is the type of Tx $\rightarrow$ LOS$\rightarrow$ Diffraction$\rightarrow$ LOS$\rightarrow$ diffraction$\rightarrow$ reflection $\rightarrow$ end. The 3D coordinates of the interacted points are collected. Euclidean distance gives the distance in between the interaction points and interaction points to UE or BS. The high level mathematical description of the METIS map-based model is given in [15]. In this section, it is briefly explained.

For a path from the transmitter element u, and the receiver element s, the set of vectors $\Psi_k = \Psi_{ki} = x_{ki}, y_{ki}, z_{ki}, T_{ki}, k = 1, \ldots K, i = 1, \ldots I_k$ needs to be determined. In which K is the number of paths ways and I_k denotes the path segments. Path segments are segments of a ray in between two interaction points. Parameters x_{ki}, y_{ki}, z_{ki} are x, y, and z coordinates of the i^{th} interaction point of k^{th} pathway, T_{ki} is the interaction type direct, reflection, diffraction, object, scattering, or diffuse scatering. The AOA and EOA can be calculated by considering the XYZ coordinates of the last interacted point and current XYZ coordinates of the UE. Similarly, the AOD and EOD can be determined using XYZ coordinates of the first interaction point and XYZ coordinates of the BS. The sum of the euclidean distance of path segments gives the total length $d_{k,u,s}$ of the ray. For each interaction, the corresponding polarization matrix A and divergence factor F need to be calculated. The polarization matrix A is a 2×2 matrix with the amplitude α in the direction θ and ϕ given as

$$A = \begin{bmatrix} \alpha_{\theta\theta} & \alpha_{\theta\phi} \\ \alpha_{\phi\theta} & \alpha_{\phi\phi} \end{bmatrix}. \tag{17}$$

The divergence factor is a measure of spreading of the wave in terms of distance. For the LOS i^{th} segment of the k^{th} path, propagation consists only the diagonal elements and it can be defined as

$$A^{los}_{k,i,u,s} = \begin{bmatrix} 1 & 0 \\ 0 & -1 \end{bmatrix}. \tag{18}$$

The corresponding divergence factor is

$$F_{k,i,u,s}^{los} = \frac{1}{s_{in}}, \tag{19}$$

where s is the length of the LOS ray. Consequently the propagation matrix $h_{k,i,u,s}$ for the full ray can be expressed as

$$h_{k,iu,s} = \beta A_{k,i,u,s}^{ref}, \tag{20}$$

where the parameter β refers to the scattered power ratio. This can be either set to a scale value or can be calculated considering the surface roughness. In each reflection case, the instruction to calculate the polarization matrix A as given in [15 p. 120].

The relation between the incident and reflected electric fields is given by

$$\begin{bmatrix} E_{\theta r} \\ E_{\phi r} \end{bmatrix} = A \begin{bmatrix} E_{\theta i} \\ E_{\phi i} \end{bmatrix}, \tag{21}$$

where $E_{\theta i}$, $E_{\phi i}$ are the incident electric fields. The electric fields at reflected fields can be calculated using the equations (5) and (4).

The parameters θ and ϕ in equation (21) denotes the polarization components in e_θ and e_ϕ directions with respect to the propagation direction e_r of the path.

In the implementation, the modelling of a diffracted ray is based on UTD or Berg's recursive model. In this thesis, it is configured as UTD. The divergence factor is expressed as

$$F^{diff} = \sqrt{s_{in}/s_D(s_{in} + s_D)}, \tag{22}$$

where s_{in} gives the distance from the BS to the diffraction point, s_D gives the distance to the UE from the diffraction point. The polarization matrix in the diffraction case is given by as

$$A = \begin{bmatrix} D_a & D_b \\ D_c & D_d \end{bmatrix}, \tag{23}$$

where D_a, D_b, D_c, and D_d are the polarization components. Reflection on rough walls is modelled as diffuse scattering. The polarization or propagation matrix for the scattered path k is given by

$$h_{k,i,us} = \sqrt{G_{k,i,us}^{sc}} \begin{bmatrix} exp(j\Phi_{k,i}^{\theta\theta}) & exp(j\Phi_{k,i}^{\theta\phi}) \\ exp(j\Phi_{k,i}^{\Phi\theta}) & exp(j\Phi_{k,i}^{\phi\phi}) \end{bmatrix}, \tag{24}$$

where $G_{k,i,us}^{sc}$ is the scattering gain and Φ is the random phase. The phases of scattered rays are modelled as the random uniform distribution with the range $[0, 2\pi]$. For the scattered rays the divergence factor of the ray can be calculated as follows

$$F^{sc} = 1/S_s, \tag{25}$$

where S_s gives the distance between the receiver node and the scattered node.

Finally, the total propagation matrix can be calculated by the product operation of the propagation matrix calculated for the each path segment. The instantaneous channel impulse response can be composed as

$$H_{u,s}(t,\tau) = \sum_{k=1}^{K} g_u^{RX}(-k_{k,u,s}^{RX}(t))^T e^{\frac{j2\pi d_{k,u,s}(t)}{\lambda}}$$

$$\cdot(\prod_{i=1}^{I_k} h_{k,iu,s}(t) F_{k,i,u,s}^{T_{ki}}(t) g_s^{TX}(k_{k,u,s}^{TX}) e^{jtw_k^D} \delta(\tau - \tau_{k,u,s}(t)), \tag{26}$$

where the antenna pattern of the u^{th} element of the receive antenna and the s^{th} element of the transmit antenna are denoted by g_u^{RX} and g_u^{TX}, the doppler frequency is denoted by w_k^D and the divergent factor of each path segment is denoted by $F_{k,i,u,s}^{T_{ki}}$ [21].

3.1.3 CloudRT - full ray tracer tool

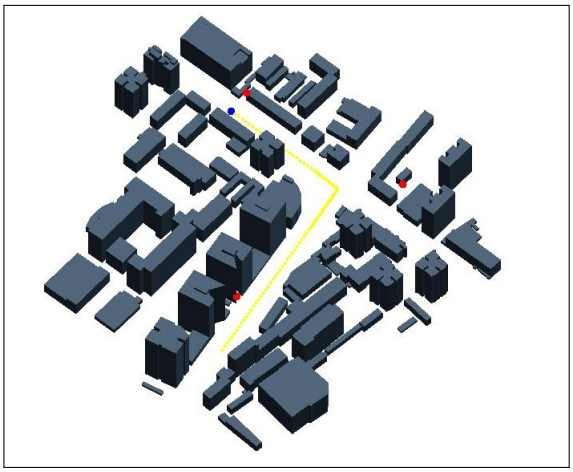

Figure 10. Map loaded to the Full ray tracing tool.

The implementation details of the CloudRT tool are discussed in [19]. In this section, the differences between the CloudRT tool and METIS map-based modelling tools are discussed. CloudRT is a high-performance computing platform. It requires coordinates of antennas, UE, building or objects. It also has an environment, material, antenna library providing the possibility to the user to customize the simulation based on the requirements. Moreover, [19] claims this RT tool can be used to simulate scenarios like mmWave railway communications and indoor mobile robots communication in smart ware-house. The differences between the METIS map-based channel modelling tool and the CloudRT tool are listed below.

- Map: METIS map-based model uses the simplified map . In the CloudRT tool the map is not altered at all.
- The material library can be used in the CloudRT tool. In the simplified map-based model, it is assumed that the all building has the same electric parameters.
- The simulation time in the CloudRT tool is significantly less than in the METIS map based tool.

- In CloudRT tool the polarization matrices cannot be derived directly. It requires 4 times simulation with the corresponding polarization configuration of the transmitter and the receiver. The configurations are HH, VV, HV, and VH.
- Penetrated rays can be modelled with the CloudRT. The current implementation of the METIS map-based model does not include this mechanism.
- METIS model supports the multiple propagation mechanism.
- Both models support up to interaction of order 3. but in the CloudRT tool it can be defined.

The following Figure 11 describes the workflow of getting the simulation data from the CloudRT tool.

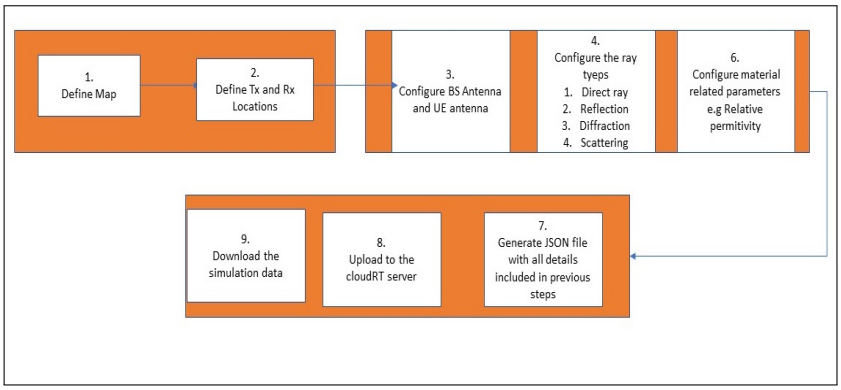

Figure 11. Workflow of generating propagation parameters from the CloudRT tool.

As illustrated in the diagram, initially the BS and the UE coordinates have to be set in the Universal Transverse Mercator (UTM) coordinate system. Antennas of the BS and the UE are configured as the isotropic antennas. Building material related parameters, such as relative permittivity, are chosen based on the material library that is set to each building. After all configuration, the configuration file is uploaded to the CloudRT server.

3.2 Map-based hybrid channel modelling

The principle of hybrid modelling is that it uses deterministic propagation parameters for the specific environment and on top of the deterministic part, the stochastic method is added to compose channel coefficients. The details on hybrid modelling are given in [22]. The map-based hybrid channel modelling was proposed in [7]. The METIS map-based model was used in the deterministic part. From the deterministic part of the METIS map-based model, the path lengths, arrival and departure directions were collected. Path tracking is considered to ensure a realistic path/cluster birth-death processes [23].

As the first step of path tracking, common paths are identified. Identifying common paths is carried out by considering the consecutive two UE locations and following the steps mentioned below.

- In each UE locations, collect the wall coordinates of the first and the last interactions.
- Compare the first and the last coordinates in the current UE positions and if the the coordinates are the same, then validate that the AOA, EOA, AOD, and EOD are the same in those UE locations in that specific interaction.
- If the above mentioned steps goes well then collect the corresponding path data.

The path tracking assures the continuity of the path. The collected paths are separated into LOS and NLOS types. The paths identified from this path tracking are considered as common paths. Initially, these common paths are grouped into clusters. The cluster centroids are chosen based on the significant paths. The clusters are selected based on the power by applying a window of 30 dB (localmax-30). The maximum number of clusters was limited to 45 in this simulation. For each cluster, cluster powers, cluster delays, and cluster angles are to be calculated. The cluster delays and powers will be the same as the delays and powers of the significant paths, of which the cluster centroids are based on. The cluster angles are calculated based on the geometric method considering the first and the last interaction coordinates. The next step is to determine the cluster angular spread. The cluster angle spreads are determined based on the path interaction type and the distance to the first and the last interaction is considered to calculate angle ranges. The cluster spread is defined as [23]

$$AS = AR/3, \tag{27}$$

where AR is the angle range. *AR* is calculated as

$$AR = 2arctan\frac{D}{2d}, \tag{28}$$

where *d* is the distance to/from the first/last interaction point. For each interaction, elevation and azimuth angular width is defined, which is then used in calculating the cluster spreads. The azimuth and elevation angle widths are presented in Table 1.

Table 1: Angle range defined for each interaction.

Interaction type	Azimuth angle width (widaz)	Elevation angle width (widel)
Ground reflection	0	0
Single reflection	3	3
Multiple reflection	7	7
Diffraction	5	10
Rooftop diffraction	10	5
Scattering	2	2
Diffuse scattering	20	20

The calculation of the cluster spreads goes as follows

$$ASD = \frac{2 * tan^{-1}(0.5 * widaz/d)}{3}, \tag{29}$$

$$ESD = \frac{2 * tan^{-1}(0.5 * widel/d)}{3}, \tag{30}$$

$$ASA = \frac{2 * tan^{-1}(0.5 * widaz/d)}{3}, \tag{31}$$

$$ESA = \frac{2 * tan^{-1}(0.5 * widel/d)}{3}, \tag{32}$$

where d is the distance to the first interaction point from the BS in ASD and ESD, and distance to the last interaction point from the UE in the ASA and the ESA. Next, on top this clusters, 20 paths were created. The power of the each ray is calculated by equally dividing the total power. The delay of rays are considered as equal to the cluster delay. The angles of the rays, such as AOA, AOD, EOD, EOA, delay and power, can be calculated. The table below shows offset that can be applied to create paths.

Table 2: Offset angles of ray .

Ray number *m*	Basis vector of offset angles α_m
1,2	$\pm$ 0.0447
3,4	$\pm$ 0.1413
5,6	$\pm$ 0.2492
7,8	$\pm$ 0.3715
9,10	$\pm$ 0.5129
11,12	$\pm$ 0.6797
13,14	$\pm$ 0.8844
15,16	$\pm$ 1.1481
17,18	$\pm$ 1.5195
19,20	$\pm$ 2.1551

The angles of the m^{th} ray of the n^{th} cluster are calculated as [24]

$$\phi_{n,m.A} = \phi_{n,A} + c_A \alpha_m, \tag{33}$$

where α_m and c_A refer to the offset of the ray and the cluster-wise angle spread. This explains the propagation channel parameters generation. Thereafter, the calculation of the fading coefficients is explained. The fading coefficients for the hybrid channel are created following the steps 11 to 13 in [3]. The fading coefficients are created for the LOS and the NLOS rays separately.

For the NLOS rays created on top of the cluster, initial phases $\Phi_{n,m}^{\theta\theta}, \Phi_{n,m}^{\theta\phi}, \Phi_{n,m}^{\phi\theta}$, and $\phi_{n,m}^{\phi\phi}$ are applied. The phase distribution follows the uniform distribution within $(-\pi, \pi)$.

The fading coefficients for the NLOS rays are composed as follows [3]

$$
\begin{aligned}
H_{u,s,n,m,k}(t) = \sqrt{\frac{P_n}{M}} \sum_{m=1}^{M} \begin{bmatrix} F_{rx,u,\theta}(\theta_{n,m,EOA}, \phi_{n,m,AOA}) \\ F_{rx,u,\phi}(\theta_{n,m,EOA}, \phi_{n,m,AOA})) \end{bmatrix}^T \\
\begin{bmatrix} exp(j\phi_{n,m}^{\theta\theta}) & \sqrt{K_{n,m}^{-1}} exp(j\Phi_{n,m}^{\theta\phi}) \\ \sqrt{K_{n,m}^{-1}} exp(j\Phi_{n,m}^{\phi\theta}) & exp(j\phi_{n,m}^{\phi\phi}) \end{bmatrix} \begin{bmatrix} F_{tx,s,\theta}(\theta_{n,m,EOA}, \phi_{n,m,AOD}) \\ F_{tx,s,\phi}(\theta_{n,m,EOA}, \phi_{n,m,AOD})) \end{bmatrix}^T \\
\cdot exp(\frac{j * 2\pi(\hat{r}_{rx,n,m}^T \cdot \bar{d}_{rx,u})}{\lambda_0} exp(\frac{j * 2\pi(\hat{r}_{tx,n,m}^T \cdot \bar{d}_{tx,u})}{\lambda_0} \\
\cdot (\sqrt{P_{n,m,k}} \cdot 10^{\frac{-(OL_{n,m(f_k + BL_{n,m}(f_{k,t}))}}{20}} exp(\frac{j * 2\pi(\hat{r}_{rx,n,m}^T \cdot \bar{v})}{\lambda_0} t
\end{aligned}
\tag{34}
$$

and the fading coefficients for LOS rays are calculated as

$$
\begin{aligned}
H_{u,s,n=1,k}(t) = \begin{bmatrix} F_{rx,u,\theta}(\theta_{LOS,EOA}, \phi_{LOS,AOA})^T \\ F_{rx,u,\phi}(\theta_{LOS,EOA}, \phi_{LOS,AOA})^T \end{bmatrix} \begin{bmatrix} exp(j\phi_{LOS}) & 0 \\ 0 & -exp(j\phi_{LOS}) \end{bmatrix} \\
\begin{bmatrix} F_{tx,s,\theta}(\theta_{LOS,EOA}, \phi_{LOS,AOA}) \\ F_{tx,s,\phi}(\theta_{LOS,EOA}, \phi_{LOS,AOA}) \end{bmatrix} exp(j2\pi \frac{f_k}{c} (\hat{r}_{rx,LOS}^T \cdot \bar{d}_{rx,u} + \hat{r}_{tx,LOS}^T \cdot \bar{d}_{tx,s})) \\
(\sqrt{P_{1,k}} \times 10^{\frac{-(OL_{n,m=1((f_k) + BL_{n,m=1}(f_k,t))}}{20}}) exp(j2\pi \frac{f_k}{c} \hat{r}_{rx,LOS}^T \bar{v} t),
\end{aligned}
\tag{35}
$$

where $F_{rx,u,\phi}$ is the field pattern of the receive antenna from the antenna element u in the direction of the spherical vectors θ and ϕ, $F_{tx,u,\phi}$ is the field pattern of the transmit antenna from the antenna element s in the direction of the spherical vectors θ and ϕ, $\bar{d}_{rx,u}$ is the location of the receive antenna element u, $\bar{d}_{rx,s}$ is the location of the receive antenna element s, $K_{n,m}$ is the cross polarization power ratio in the linear scale, and v is the doppler frequency.

4 CHANNEL MODEL EVALUATION METRICS

From legacy systems to 5G and beyond channel modelling has evolved by requiring the knowledge about the channel in power, frequency/delay, time/doppler, spatial or angular and polarimetric domain [25]. The knowledge of the behavior of the channel in these domains is needed to design a high performing communication system. The multipath signal that is transmitted from an antenna is received with different delays, distance, and direction. The study of the dispersion of received signal in these domains is essential to know the negative impact of multipath propagation in the NLOS condition.

4.1 Power delay profile (PDP)

The power delay profile depicts the variation of the power of each path with respect to the delay. In this simulation, it is presented as power and delay variation along the UE positions. As this simulation deterministic based, power, and delays are one of the direct outputs from the three channel models.

4.2 RMS delay spread

The multipath propagation has introduced many rays and each ray has the different gain and delay. The knowledge of the delay spread is essential to know whether a channel is ISI-free channel or not. RMS delay spread is one of the techniques that is used in characterizing the wideband channel [26]. The standard deviation and the mean of the delay spread are calculated as [27]

$$DS = \sqrt{\frac{\sum_{=1}^{M} P_m \tau_m^2}{\sum_{m=1}^{M} P_m} - \tau_0^2}, \tag{36}$$

where P_m and τ_m refer the power and the delay of the m^{th} path. The mean delay τ_0 is defined as

$$\tau_0 = \frac{\sum_{m=1}^{M} P_m \tau_m}{\sum_{m=1}^{M} P_m}, \cdot \tag{37}$$

4.3 RMS angle spread(circular angle spread)

The angle spread calculation shows the dispersion of the received signal in the angular domain. The channel with a large angular spread shows large capacity and the small angular spread assists in efficient beamformer design [28]. The properties of the angular spread are claimed to govern the characteristics of capacity distribution and eigenvalues [29]. There are two methods that have been discussed in the literature to find the angle spreads [30]. One method considers the LOS path as a reference and calculate spreads but the other method uses a circular wrapping method to find the

reference direction. In this thesis, the latter method is used. The CAS function as described in [31], can be calculated for N multipaths and each having M sub-paths

$$\sigma_{AS} = \sqrt{\frac{\sum_{n=1}^{N}\sum_{m=1}^{M}\left(\theta_{n,m,\mu}\right)^{2} * P_{n,m}}{\sum_{n=1}^{N}\sum_{m=1}^{M} P_{n,m}}}, \tag{38}$$

where $P_{n,m}$ is the power of m^{th} sub-path of the n^{th} path. $\theta_{n,m,\mu}$ is defined as

$$\theta_{n,m,\mu} = mod(\theta_{n,m} - \mu_{\theta} + \pi, 2\pi) - \pi\cdot \tag{39}$$

The symbol μ_{θ} is expressed as

$$\mu_{\theta} = \frac{\sum_{n=1}^{N}\sum_{m=1}^{M}\theta_{n,m} * P_{n,m}}{\sum_{n=1}^{N}\sum_{m=1}^{M} P_{n,m}}, \tag{40}$$

where $\theta_{n,m}$ is either the AOA or the AOD of the m^{th} sub-path of n^{th} path.

4.4 Power angular spectrum (PAS)

Power angular spectrum gives the power distribution in the angular domain. It is an essential metric to know the direction of power where the maximum power is generated in the angular domain.

4.5 Cross-polarization power ratio

Cross-polarization measure provides the knowledge about the polarization imbalance. The ray experiences different interactions while travelling from the transmitter to the receiver and the polarization of the ray is changed in each interaction. Therefore, it is necessary to know the power in the polarization domain in order to know the power loss due to polarization mismatch. The calculation of the polarization ratio is mainly carried out for isotropic antennas. The cross-polarization ratios XPRv, XPRh are defined in [32] as

$$XPR_{V} = \frac{|\alpha^{VV}|^{2}}{|\alpha^{HV}|^{2}}, \tag{41}$$

$$XPR_{H} = \frac{|\alpha^{HH}|^{2}}{|\alpha^{VH}|^{2}} \tag{42}$$

where α is the amplitude, vv, vh, hv, and hh denotes the polarization of the transmitter and the receiver antennas. XPRv is a measure of the power at vertically polarized antenna in its orthogonal polarized direction and XPRh is defined as vice versa. The equations (41) and (42) are defined for the calculation at the receiver.

4.6 K-factor

The K-factor is a measure of ratio of the power between the LOS ray and the NLOS ray. In a study by [33], it was found that, by increasing the use of higher bands and access point density, there is an increase of the LOS condition and the K-factor is said to influence the fading statistics of BER, spectral efficiency, level crossing rate, and average fading duration. K-factor can be calculated as [34]

$$KF = \frac{P_{LOS}}{\sum_{m \neq LOS} P_m}, \tag{43}$$

where P_{LOS} is the power from the LOS ray and m is the number of rays.

5 SIMULATION AND RESULTS

This chapter introduces the scenario, the channel model configurations and the comparison results of the modelled channel characteristics. The objective of this work is to model the propagation channel in this chosen environment. This thesis does not asses the capability of a modelling tool or to point out a certain weakness in the modelling tool.

5.1 Channel modelling settings

In the literature, one of the 5G deployment scenarios is urban micro (UMi) with outdoor to outdoor (O2O) propagation [24]. The urban street canyon scenario type environment was chosen to model the channel. The 3D map of the corresponding environment is presented in Figure 12. The UE route and the locations for the base stations were selected with the possibility to have the LOS and the NLOS propagation condition. The UE route drawn with red and yellow colour was chosen to model the channel. The UE route is discretized into 97 points with 5 m (red line) and 2.5 m (yellow line) space as shown in Figure 12. In this thesis the following terms are used: 1) METIS refers to the ray tracing based modelling tool with the simplified map implemented in the METIS project, 2) FULLRT refers to the so-called CloudRT software which is based on full ray tracing, which was implemented by Beijing Jiaotang University, and 3) HYBRID refers to the METIS map-based model based hybrid implementation developed by Keysight Finland Technologies Oy. In addition to this, the LOS UE positions means the UE positions with the LOS condition and the NLOS UE positions means the UE positions without the LOS condition.

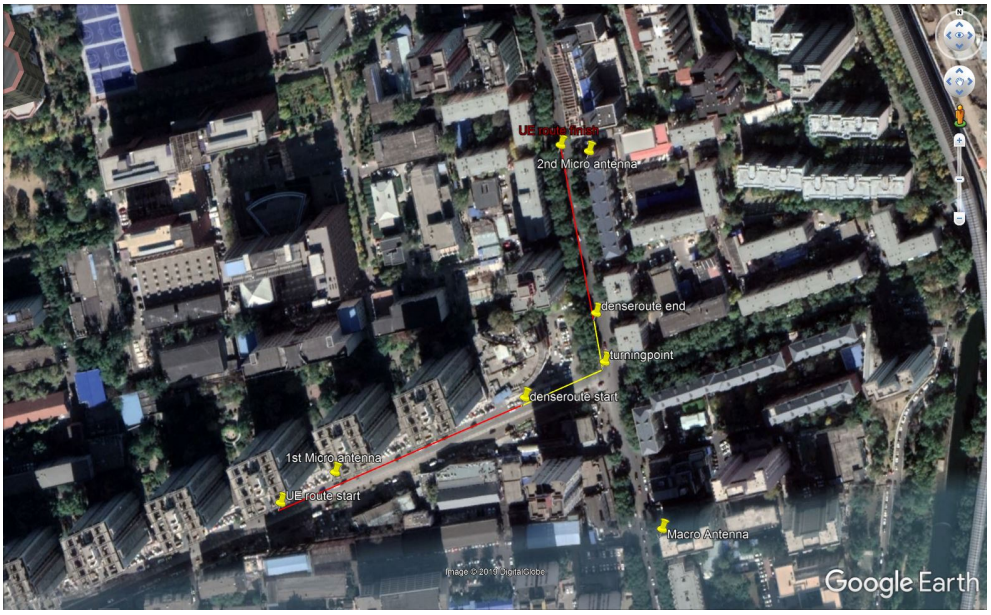

Figure 12. 3D view of map and including the positions of the UE and the base stations.

In Figure 12, two micro base stations with the height 14 m and one macro base station with the height 60 m are deployed as shown. These base stations are addressed with the names BS1, BS2, and BS3, respectively. In addition to that, Table 3 and 4 shows the other parameters used to generate the channel model in both modelling tools.

Table 3: The parameters in the METIS map-based channel model configuration.

Parameter	**Settings**
Absorption coefficient α	0
Specular/Diffuse power ratio	0.5
Relative permittivity ϵ	4.5
Carrier Frequency	3.5 GHz

Table 4: The parameters in the FULLRT based channel model configuration.

Parameter	***Settings***
Relative permittivity ϵ	1.91
Loss tangent	0.0296
Directive S	0.00187
Directive Alpha	50
Career Frequency	3.5 GHz

5.2 Simulation results

The simulations results consist of the comparison of both the large scale and the small scale characteristics of the three channel models for the three scenarios. The compared channel characteristics are the number of paths, LOS and NLOS UE positions, path loss, delay spread, statistics of angles, angle spreads, and the K-factor.

5.2.1 The LOS and NLOS UE positions

It is essential in a ray tracing based model to discover the propagation condition for a specific UE location. The propagation conditions in the hybrid model is identical to the METIS model, hence it was decided to skip hybrid model in this comparison. The LOS and the NLOS UE positions in the three scenarios are presented in Table 5 and the corresponding UE locations are depicted in Figures 13,14, and 16.

Table 5: LOS positions in all three base stations.

	METIS	FULLRT
BS1	$1 \rightarrow 67$	$1 \rightarrow 67$
BS2	$48 \rightarrow 97$	$44 \rightarrow 97$
BS3	$1 \rightarrow 16$, $30 \rightarrow 97$	$30 \rightarrow 97$

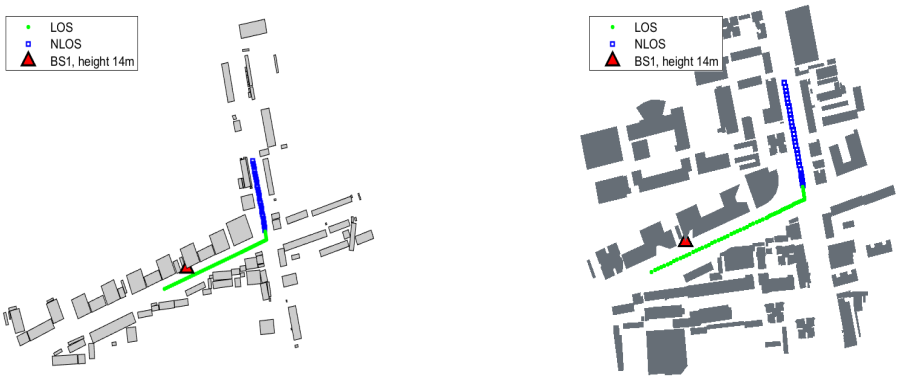

(a) (b)

Figure 13. UE positions with the LOS and the NLOS condition in the BS1 scenario with the height 14 m : (a) METIS map-based model, (b) FULLRT based model.

Figure 13 depicts the LOS and the NLOS conditions in the UE positions. In this scenario, both models have the same UE positions with the LOS conditions, which are at the first 67 UE positions. However, this situation is changed in other two scenarios.

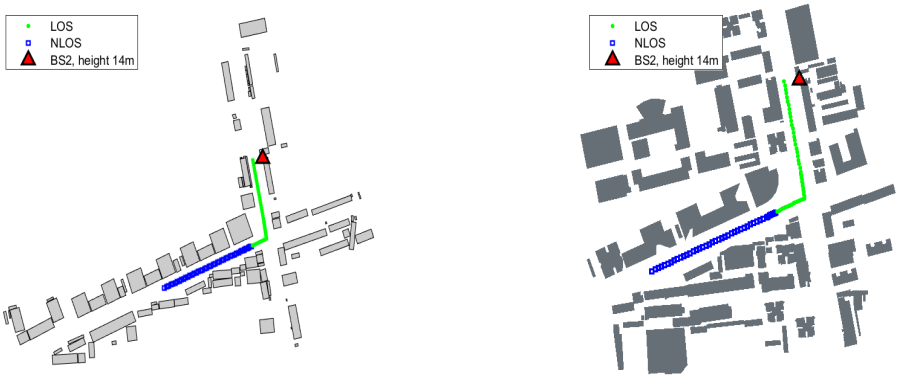

(a) (b)

Figure 14. UE positions with the LOS and the NLOS conditions in the BS2 scenario with the height 14 m: (a) METIS map-based model, (b) FULLRT based model.

Figure 14 illustrates the LOS and the NLOS positions that were in the BS2 scenario. Mismatches in the LOS condition can be seen. Table 5 shows that the UE positions from 48 to 97 has the LOS conditions in the METIS model and the UE positions from 44 to 97 in the FULLRT model has the LOS conditions. The reason for this mismatch is due to the simplifying approach, which is explained in Figure 15.

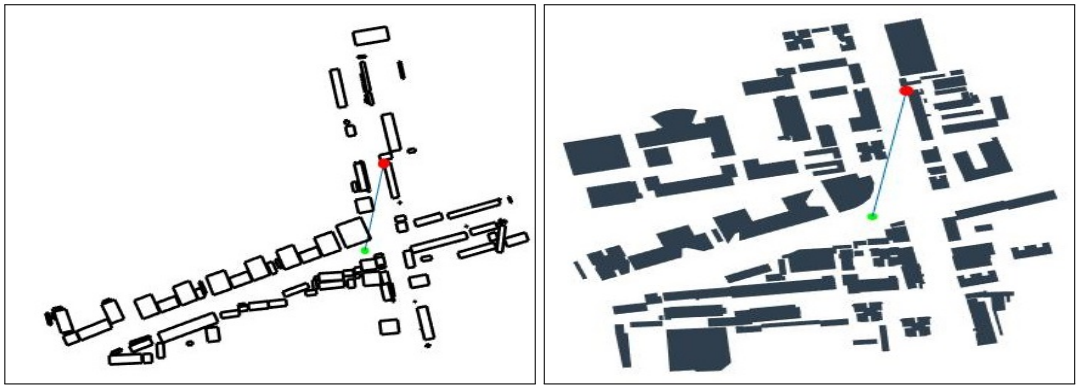

(a) (b)

Figure 15. Illustration of the line from the micro BS2 to the 47^{th} UE position: (a) METIS map-based model, (b) FULLRT model.

It is seen that the geometry of the building is changed and hence it blocks the direct ray at that specific UE position in the METIS model. The number of the LOS conditions are increased for the BS3 scenario. But there were mismatches due to the same reason as in the BS2 scenario. Figure 16 depicts the propagation conditions at each UE positions in the BS3 scenario.

(a) (b)

Figure 16. UE positions with the LOS and the NLOS conditions in the BS3 with the height 60 m : (a) METIS map-based model, (b) FULLRT based model.

The height of the BS3 is 60 m and it is obviously the reason for the increase in the positions with the LOS conditions. In the METIS model, the UE positions from 1 to 16 and 30 to 97 have the LOS conditions, whereas in the FULLRT model the positions 30 to 97 have LOS conditions. The comparison of this result reveals that simplifying buildings definitely has a negative effect but it is also needs to be mentioned that it is hard to over come such issue when doing the simplifying process.

5.2.2 Number of paths

This section presents the number of paths comparison. The comparison is carried out by considering a dynamic range in each UE locations in order to observe the percentage of the strong paths among all paths. The dynamic range are calculated by considering the 60 dB threshold from the highest power of the ray in each locations. The total paths and the paths within the dynamic range are presented by the dark red colour and the blue colour, respectively. The difference in the total paths does not mean the capability of the modelling software, rather is constraint of the system, However, the paths within the DR are essential to know the percentage of the stronger paths in each location. The number of paths modelled in each 97 UE position in BS1, BS2, and BS3 scenarios are displayed in Figures 17, 18, and 19 respectively.

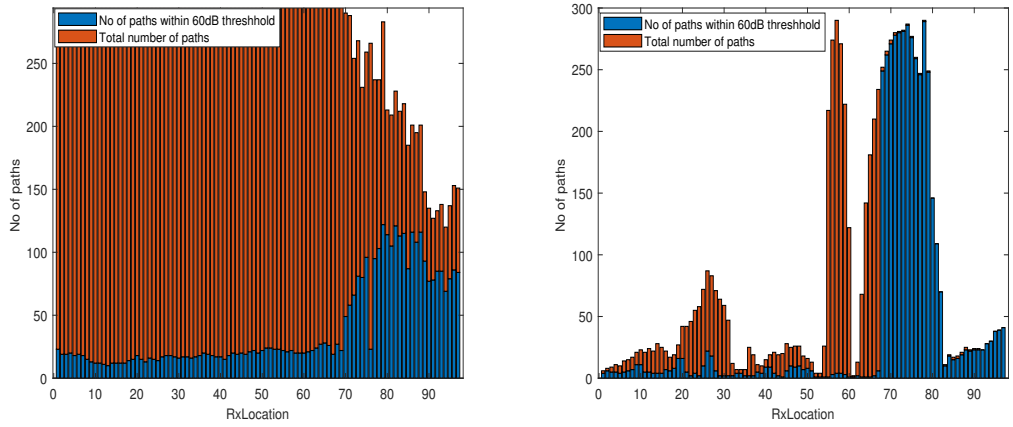

Figure 17. The number of paths in the BS1 scenario : (a) METIS map based model, (b) FULLRT based model.

The maximum of the total paths are 850 and 290 in the METIS model and the FULLRT model respectively. The paths within the dynamic range vary in each location. In the LOS UE positions it ranges between 5 to 10 and 1 to 5 in the METIS model and the FULLRT model, respectively. Interestingly, all paths in the NLOS UE positions in the FULLRT model lies within the range but it does not necessarily mean the paths powers are strong but those path powers are below -140 dB. The reason for less number of paths within DR in the LOS UE positions is the LOS path has much strong power compared to the NLOS paths.

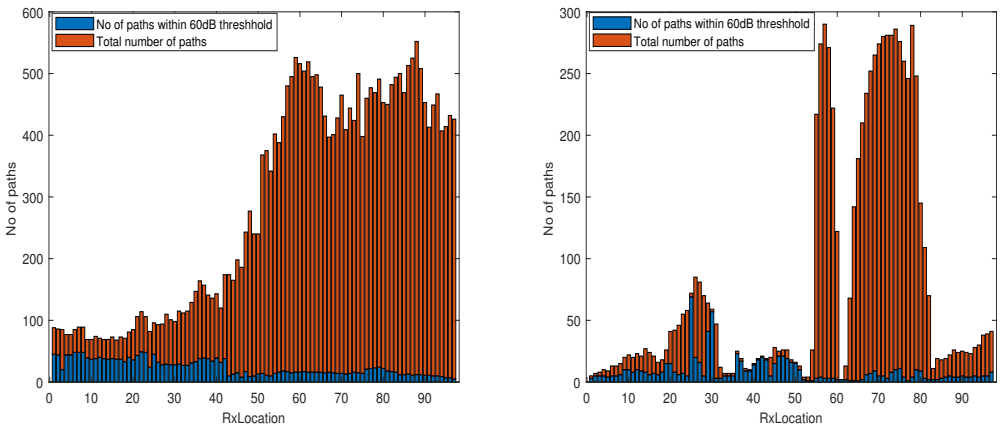

Figure 18. The number of paths in the BS2 scenario : (a) METIS map based model, (b) FULLRT based model.

Figure 18 presents the number of paths in the BS2. The variation of the number of paths has the similar nature as in the BS1 scenario. But in this case the NLOS positions of the FULLRT model shows less number of total paths and paths within DR are less than what is in the BS1 scenario. This difference implies that, though the scenario is same, statistics do not need to be the same as the antenna location is different and the rays encounter different interactions. The paths in the BS3 scenario are shown in Figure 19.

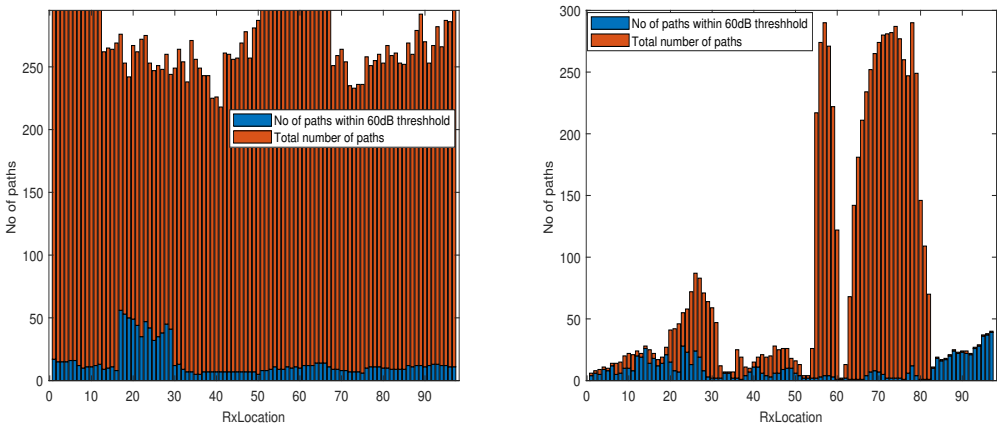

Figure 19. The number of paths in the BS3 scenario : (a) METIS map based model, (b) FULLRT based model.

Even though antenna height is large, the number of paths are less than the number of paths in the UMi scenario, but interestingly the paths within DR are higher than in the UMi scenario. It is also needs to be noted that the NLOS positions in the METIS

model have maximum power of the ray around -118 dB which is higher than the maximum power of the ray in the NLOS positions in the UMi scenario. This comparison reveals, the influence of the height of the antenna in the power of the NLOS rays in the UE positions that do not have the LOS conditions. Two discrete reasons can be put forwarded as the reasons for less number of the paths within the DR in the FULLRT model. They are, reflection of order 2 and the rays that do not have the multiple propagation mechanism combined together.

5.2.3 Path loss comparison of the three scenarios

The gain of the antennas, the other losses such as antenna feeder loss are not considered in the calculation. The path loss of the hybrid model is skipped as it takes the propagation parameters of the METIS model and therefore the path loss is identical to the METIS model. The free space path loss (FSPL) is calculated based on the Frii's law [35] for reference.

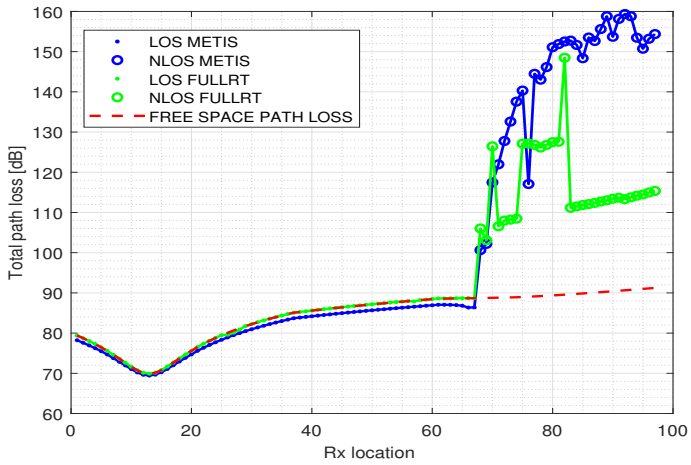

Figure 20. Path loss comparison at 3.5 GHz in the BS1 scenario.

Figure 20 shows the total path loss calculated at each in the UE location in the BS1 scenario. In addition to that, FSPL has been plotted as the reference. In the UE Locations, where the LOS condition or the LOS path exists, the total loss includes the loss from the LOS path and the other multipath. Therefore, the total loss has to be less than FSPL as there are gain in the multipath. In all three scenarios, in the UE positions where the LOS condition exists, the METIS model shows 2 dB gain but the FULLRT model almost follows the FSPL as the multipath are weak. This is also illustrated in Figure 23, which presents the different between the FSPL and the total path loss.

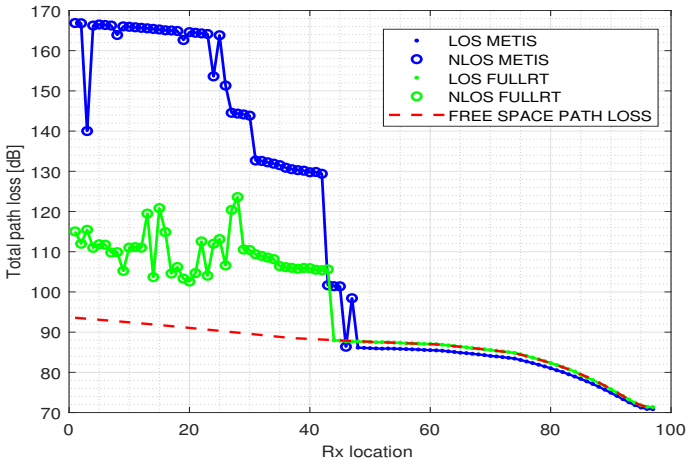

Figure 21. Path loss comparison at 3.5 GHz in the BS2 scenario.

The path loss in the BS2 scenario has the same trend as in the BS1 scenario at the UE positions where the LOS condition exist. However, the total loss is very high in the METIS model at the UE positions where the LOS condition does not exist.

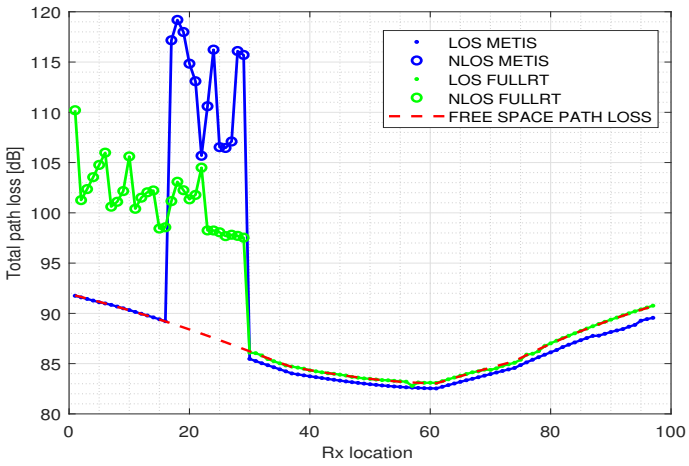

(a)

Figure 22. Path loss comparison at 3.5 GHz in the BS3 scenario.

In the BS3 scenario, the UE positions where the both model has the NLOS propagation condition, the loss is considerably less than in the BS1 and BS2 scenarios. It is observed that the METIS model has around 15 dB higher loss than the FULLRT model.

The path loss values at the UE positions where the LOS condition does not exist have dramatic discrepancies. This also can be said due to the differences in the modelled NLOS rays. Next, the comparison of the path loss to FSPL is presented. The "path loss to FSPL" is calculated by subtracting the total loss from the FSPL. At each location, the FSPL was calculated regardless of the propagation condition. The purpose of this comparison is to illustrate the loss variation along the UE locations with respect to the

FSPL. In the UE locations with the LOS propagation condition, the result of subtracting the FSPL loss from total loss can be considered as the gain. It is because the loss of the LOS ray can be calculated with FSPL. The positive result is represented by the dark red colour.

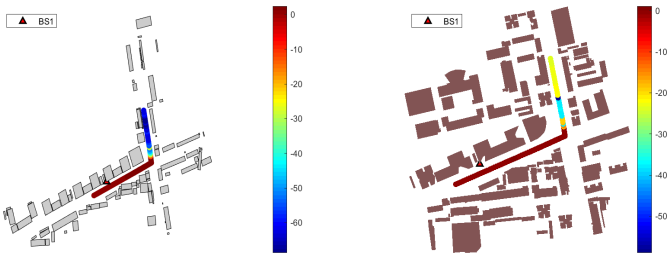

(a) (b)

Figure 23. Path loss to FSPL comparison in the BS1 scenario : (a) METIS, (b) FULLRT.

Figure 23 shows the colour which represents the gain in the LOS UE positions. This implies that the NLOS rays of the METIS model in the LOS UE positions have higher power than the NLOS rays of the FULLRT model.

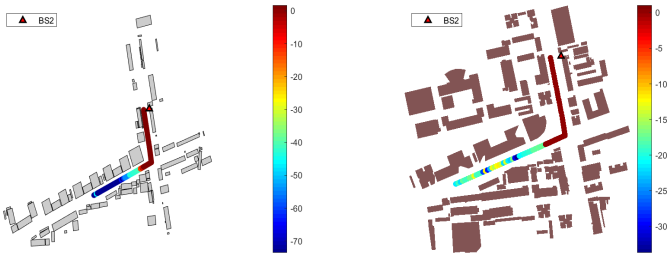

(a) (b)

Figure 24. Path loss to FSPL comparison in the BS2 scenario : (a) METIS, (b) FULLRT.

Figure 24 depicts the BS2 results for the path loss to FSPL comparison. This shows the similar trend as in the BS1 scenario. However, it is observed that the METIS model has a higher loss in the NLOS UE positions.

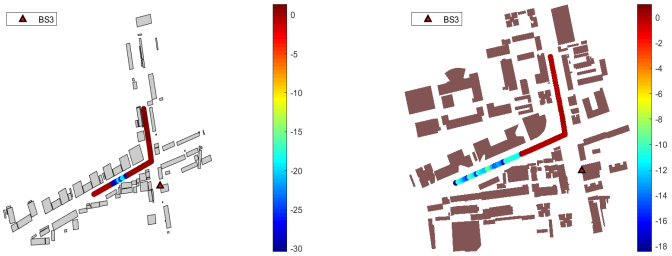

(a) (b)

Figure 25. Path loss to FSPL comparison in the BS3 scenario : (a) METIS, (b) FULLRT.

In the BS3 scenario, also the similar trend in BS1 and BS2 scenarios is exhibited.

In summary, the NLOS UE location has dramatic discrepancies between both models. The reasons identified are similar to that discussed in the number of paths comparison. The propagation condition mismatch between the models and the rays from the FULLRT model does not include the rays combined with more than one propagation mechanism.

5.2.4 Power delay profile (PDP)

The power delay profiles in the BS1, BS2, and BS3 scenarios are presented in Figures 26, 27, and 28, respectively. The height of the vertical lines are negatively proportional to the delays and colours of the lines are used in a way the rays can be distinguished based on the power. In each UE locations, the rays with the power below the 200 dB were discarded.

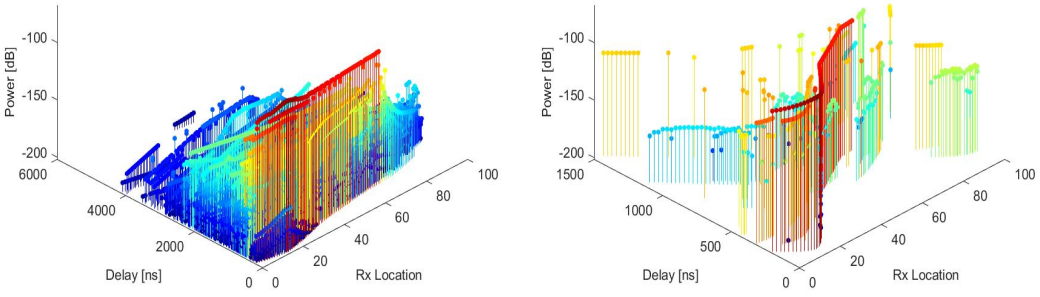

(a) (b)

Figure 26. Power delay profile in the BS1 scenario : (a) METIS, (b) FULLRT.

The PDP comparison in the BS1 scenario between the METIS and the FULLRT model shows the similar trend in the LOS UE locations. However, in the NLOS UE locations, the delays of stronger rays vary dramatically. It is clearly seen that the NLOS rays in the NLOS UE location of the FULLRT model have stronger power than the METIS model. Next, the PDP in the BS2 scenario is presented in Figure 27.

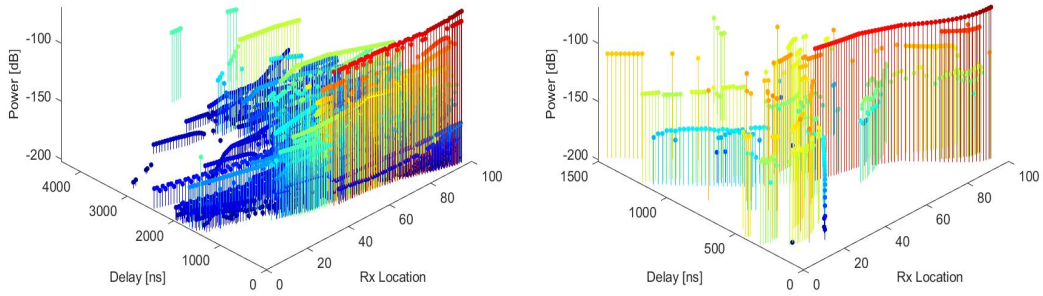

(a) (b)

Figure 27. Power delay profile in BS2 scenario : (a) METIS, (b) FULLRT.

In BS1 and BS2 scenarios, it is surprising to see in the NLOS UE locations, there are differences in the delays of the rays with the stronger rays. The PDP in the BS3 scenario is presented in Figure 28.

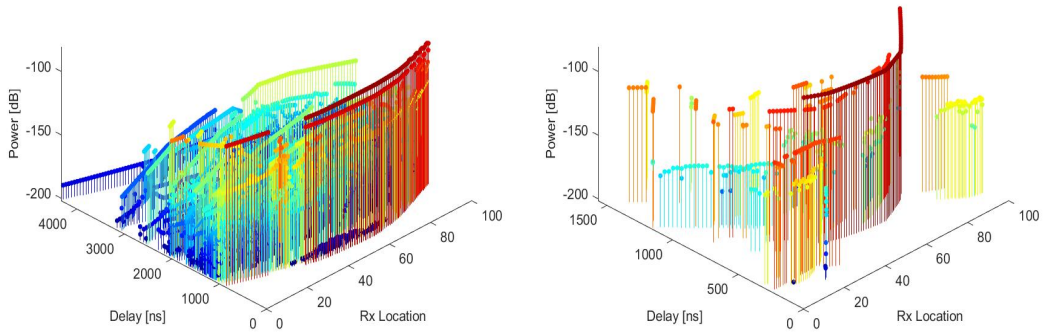

(a) (b)

Figure 28. Power delay profile in the BS3 scenario : (a) METIS, (b) FULLRT.

In the BS1, BS2, and BS3 scenarios, the results of the LOS rays as anticipated. However in the METIS model it is observed to see the higher number of rays with longer delays and significantly low powers.

5.2.5 K-factor comparison

The K-factor is calculated in the UE locations that have the LOS condition. The K-factor results in the BS1, BS2, and BS3 scenarios are presented in Figures 29, 30, and 31. The K-factor values have dramatic discrepancies in all three scenarios. Firstly, the *KF* in the BS1 scenario is analyzed.

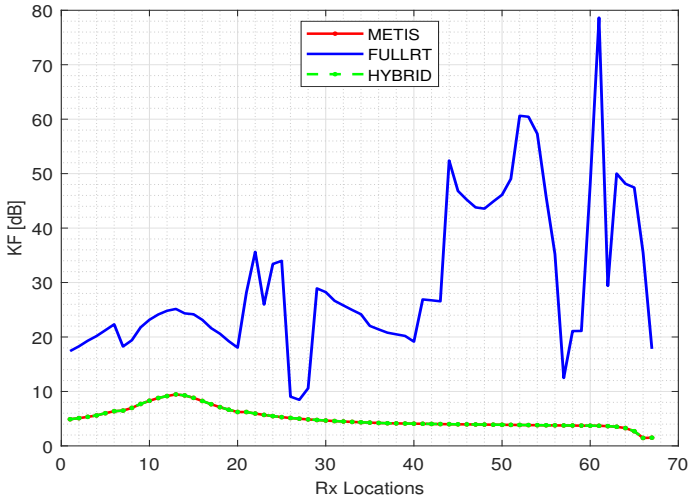

Figure 29. K-factor comparison in the BS1 scenario.

The *KF* of the METIS model and the HYBRID model shows consistent and well-aligned between two models. The *KF* of the METIS model in the BS1 scenario starts from 5 dB and reach a peak at the 12^{th} position and reduce gradually and reaches around 2 dB at the 67^{th} position. Next, the *KF* in the BS2 scenario is presented.

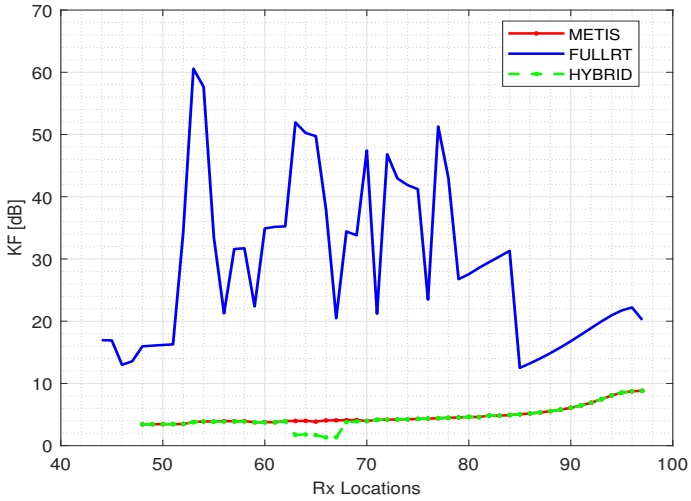

Figure 30. K-factor comparison in the BS2 scenario.

In the BS2 scenario, it starts at 4 dB and increases gradually until the last position. This trend in UMi implies that, the higher *KF* is reflected at the UE positions with higher euclidean distances. Thirdly, the *KF* result in the BS3 is discussed.

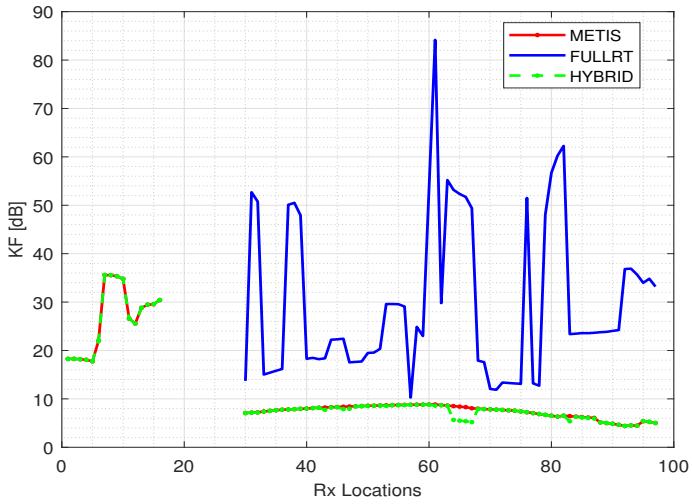

Figure 31. K-factor comparison in BS3 scenario.

At first 18 positions in the BS3 scenario, the *KF* values of the METIS model have rise and fall and from the 30^{th} UE position shows similar trend in the UMi scenario. One unanticipated finding is that the *KF* of all three BSs in the FULLRT model, fluctuates frequently. These results did not show a significant trend. One immediate conclusion can be derived is that, the power of the NLOS rays at the each UE locations in the FULLRT model are significantly weak. In addition to that the ground reflected rays were not observed in the FULLRT model. Since the attenuation is mainly caused by the distance travelled by the ray and the FULLRT model has limited support of propagation mechanism, the NLOS rays from the FULLRT model fail to find the NLOS rays that are possible to reach the UE with shorter distance. Therefore, this could be the reason for the higher *KF* in the FULLRT model.

5.2.6 Statistics of angles comparison

This section consists of the study of the probability of azimuth angles of arrival, azimuth angles of departure, elevation angles of arrival, and elevation angles of departure. We considered 5^o angle bin size to calculate probability. Firstly, the probabilities of AOAs in the BS1, BS2, and BS3 scenarios are presented in Figures 32, 33, and 34.

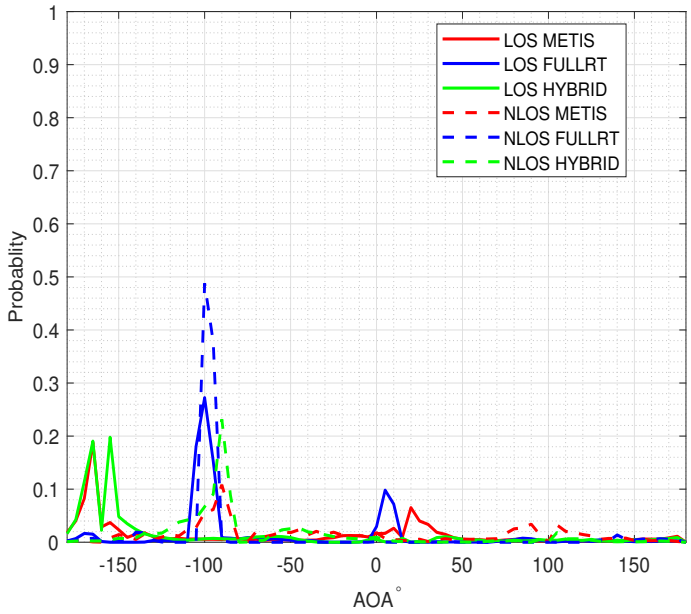

Figure 32. Probability of azimuth of angle of arrival in the BS1 scenario.

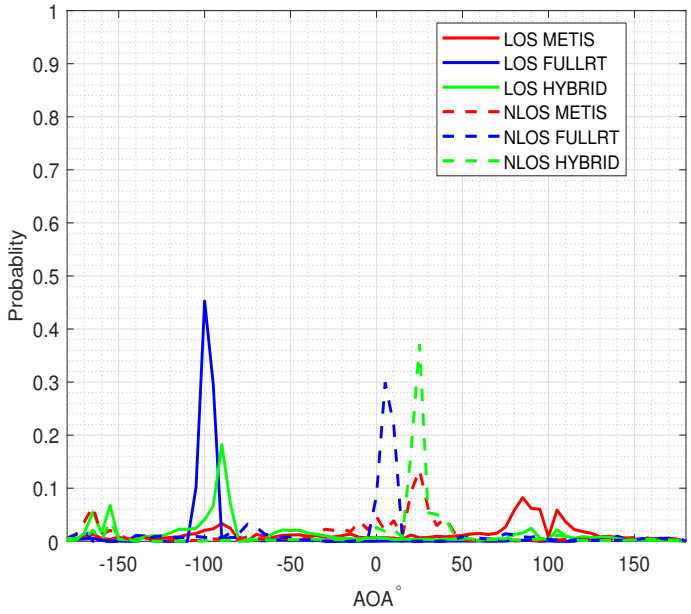

Figure 33. Probability of azimuth of angle of arrival in the BS2 scenario.

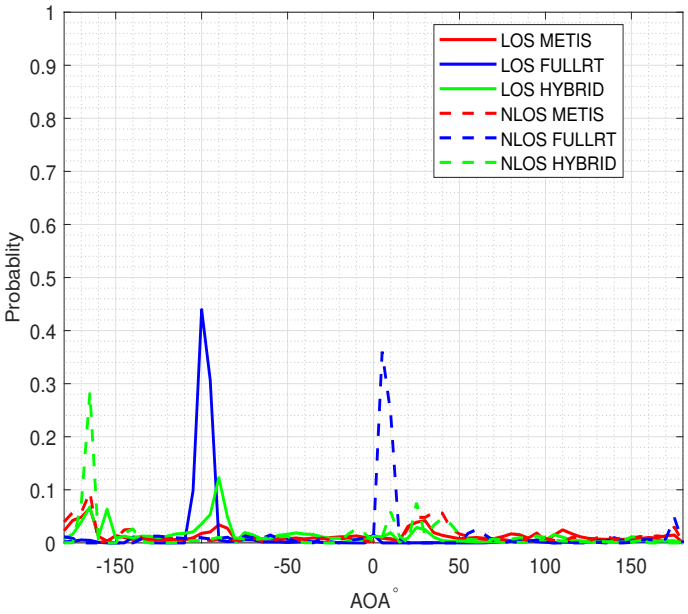

Figure 34. Probability of azimuth of angle of arrival in the BS3 scenario.

Though the BS1 and the BS2 are UMi with the same height 14 m, they do not show considerable similarity in the statistics of AOA. In the BS1 scenario, the rays arrive with the azimuth angles $-100°$ and $-5°$ in the FULLRT model but in the METIS model, there are azimuth angles $-160°$ with the 0.2 probability and $-25°$ with 0.8 probability. FULLRT model yield same azimuth angles in all scenarios. The rays in the HYBRID model arrive with multiple azimuth angles. The azimuth angles observed in the BS1 scenario are $-160°$, $-100°$, in the BS2 scenario, angles are $-90°$, $250°$ and in the BS3 scenario, the angle is $-160°$. Despite of these dissimilarities in the probability of AOA, it is more interesting to see there are higher probabilities of elevation angles with similarities. Secondly, the EOAs in the BS1, BS2, and BS3 scenarios are presented in Figures 35, 36, and 37.

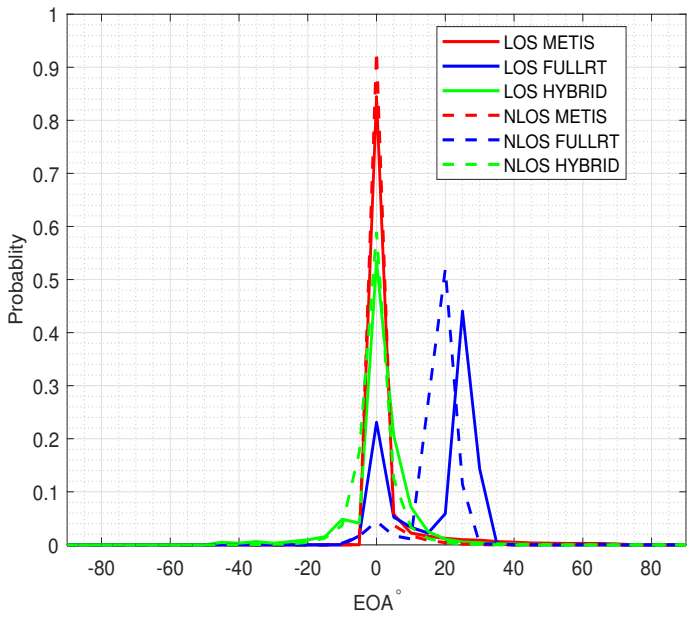

Figure 35. Probability of elevation of angle of arrival in the BS1 scenario.

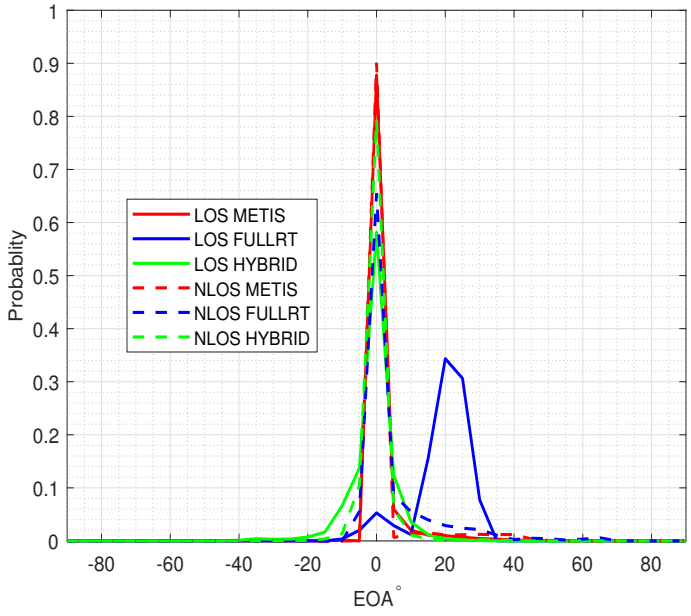

Figure 36. Probability of elevation of angle of arrival in the BS2 scenario.

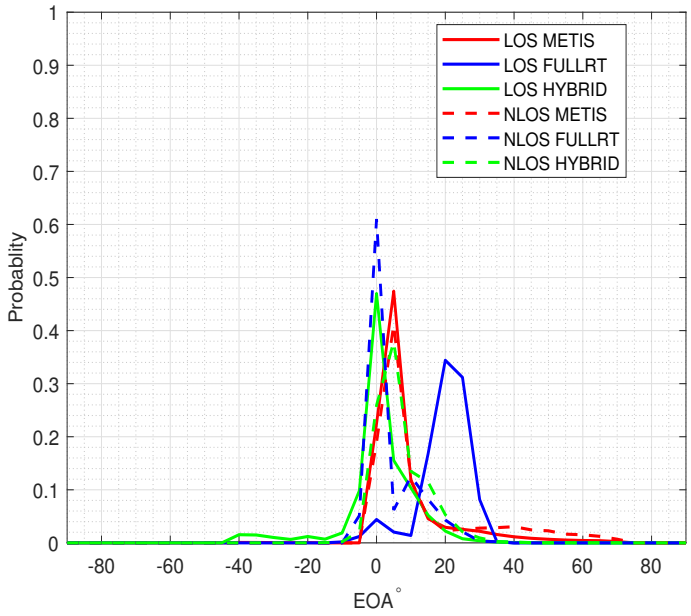

Figure 37. Probability of elevation of angle of arrival in the BS3 scenario.

The elevation angles of arrival are identical in both the METIS and the HYBRID. The EOA in this case is centered around $0°$. Surprisingly, in the BS3 scenario, the EOA is increased to almost $5°$. However, the EOAs in the FULLRT model shows different values than the other two models. Thirdly, the statistics of the AODs are discussed in Figures 38, 39, and 40.

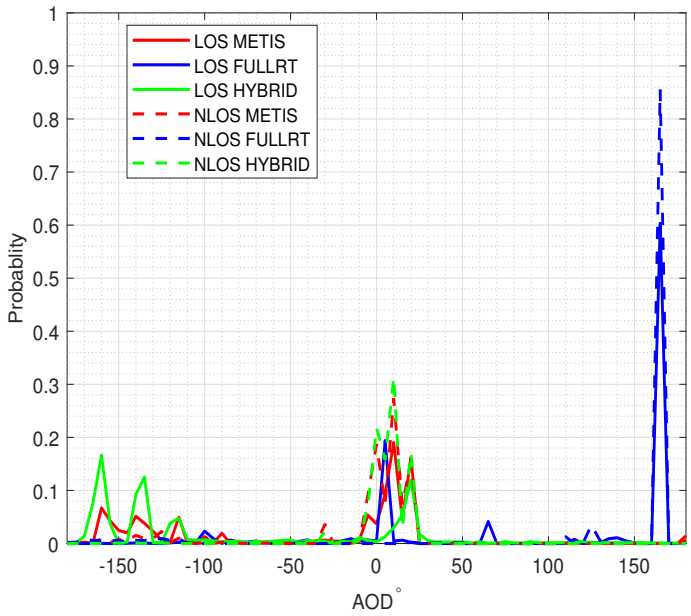

Figure 38. Probability of azimuth of angle of departure in the BS1 scenario.

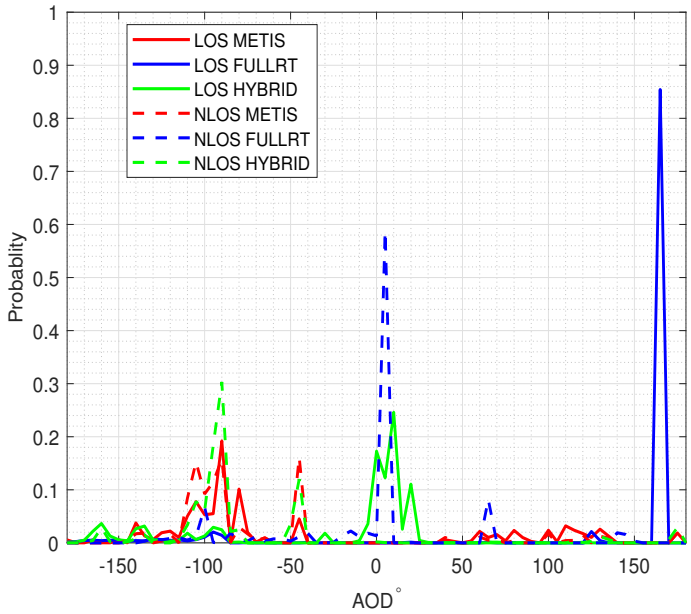

Figure 39. Probability of azimuth of angle of departure in the BS2 scenario.

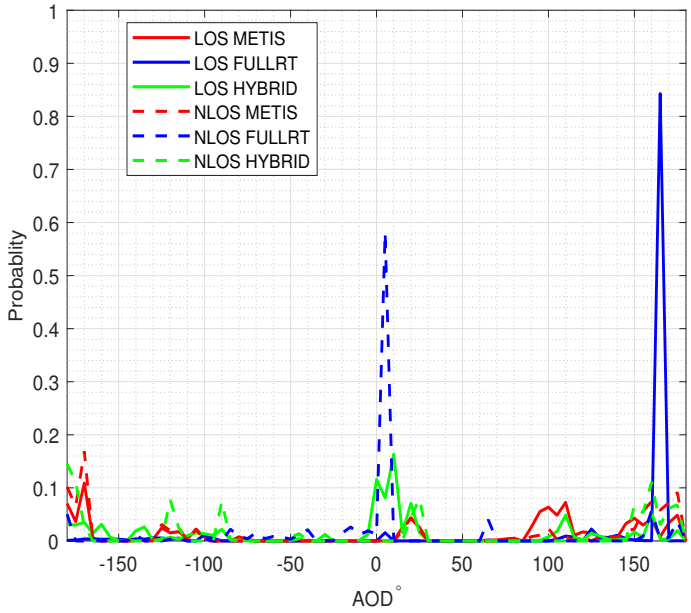

Figure 40. Probability of azimuth of angle of departure in the BS3 scenario.

The azimuth angles of departure from the BS1 scenario in the HYBRID and the METIS models are $-160°$, $10°$, and the BS2 scenario angles are around $90°$ and $10°$. However, it needs to be noted the probabilities of same angles are less than in the HYBRID model. It is difficult to draw any conclusion about the angles in the BS3 scenario, as there are not any considerable peaks in probabilities. Interestingly, angles in the FULLRT models shows higher probability for $10°$ and $160°$. It is surprising to see the angle $160°$ in the FULLRT model. Unlike the azimuth angles of departure,

there are similarities seen in the elevation angles of departure. The EOD is illustrated in Figures 41, 42, and 43.

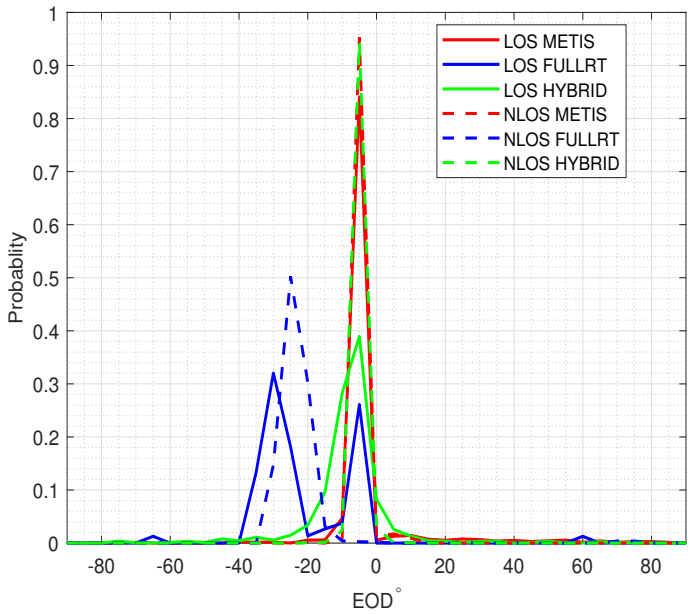

Figure 41. Probability of elevation of angle of departure in the BS1 scenario.

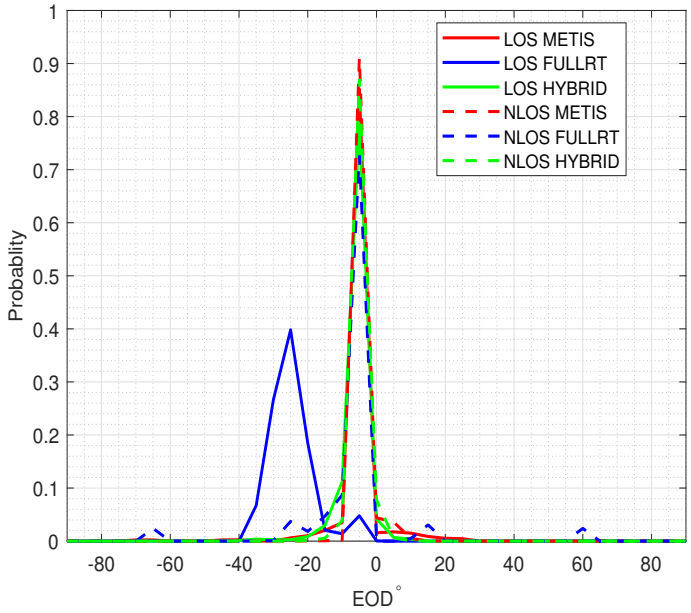

Figure 42. Probability of elevation of angle of departure in the BS2 scenario.

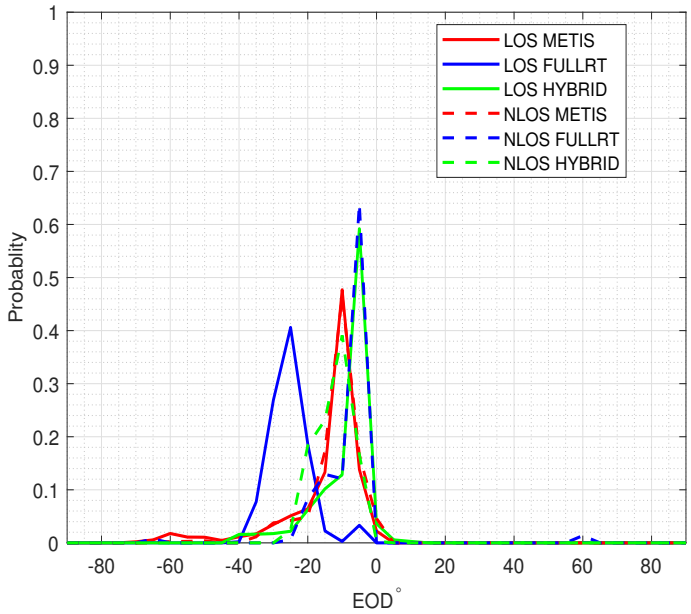

Figure 43. Probability of elevation of angle of departure in the BS3 scenario.

In all three scenarios -5° is a common angle. Similar to other cases the METIS model elevation angles are analogous to the HYBRID model. Unlike EOA and EOD shows a negative shift in angles and there is a probability of -5° departure angles.

In summary, the azimuth angles of both the arrival and the departure angles from the METIS and the HYBRID model gives multiple angles but the FULLRT model gives less number of angles. Though there are few similarities in the elevation angles, there are considerable shifts seen in the angles of the FULLRT model. The last and the first interaction point influence the angles. It could be argued that the differences in the features of the modelling tool, such as supported mechanisms cause these discrepancies.

5.2.7 Angle spreads comparison

The measure of angle spreads provides the knowledge about the dispersion of the power of the rays in the spatial domain. The comparative analysis of the angular dispersion of arrival and direction angle in the azimuth and the elevation domain is presented. Firstly, the ASA of the BS1, BS2 and BS3 scenarios are illustrated in Figures 44, 45, 46.

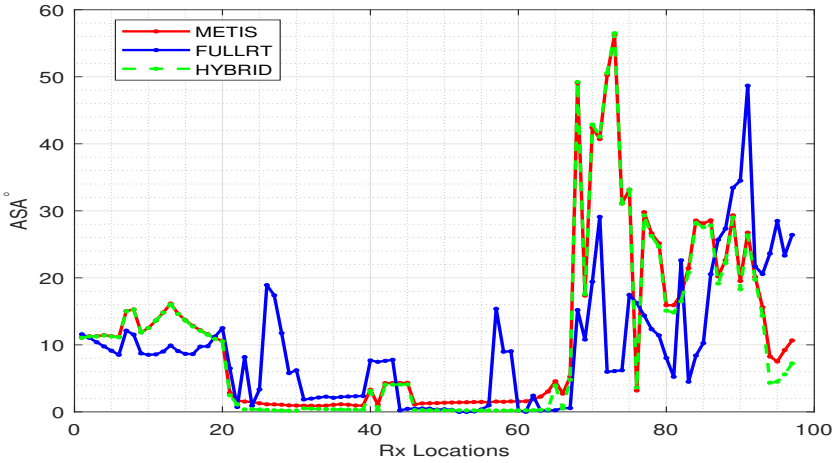

Figure 44. ASA in the BS1 scenario.

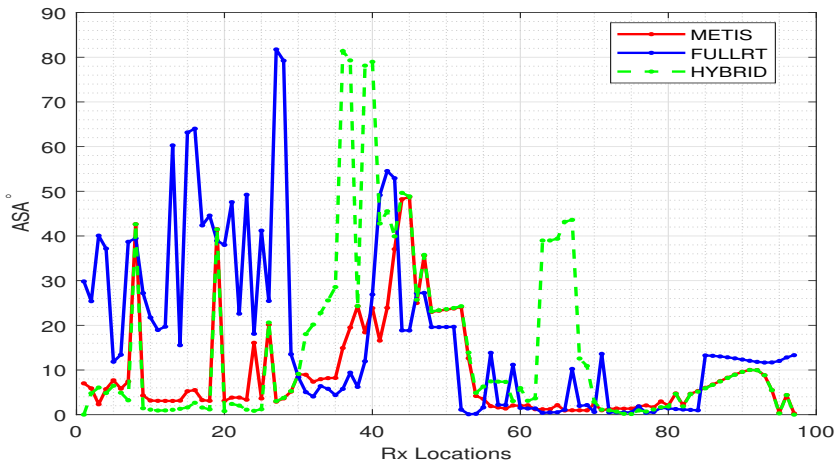

Figure 45. ASA in the BS2 scenario.

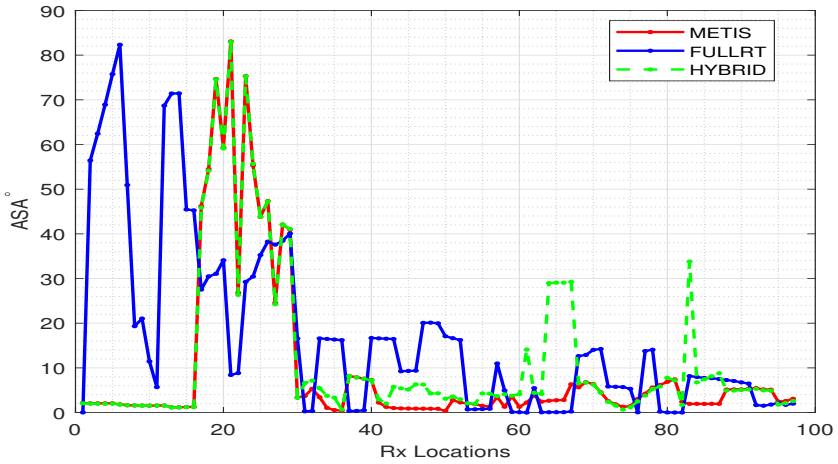

Figure 46. ASA in the BS3 scenario.

In Figure 44, the first twenty positions shows similar spreads values. From the 20^{th} position to the 67^{th} position, the ASA of the METIS and the HYBRID models go near to 1° and the FULLRT model shows inconsistent values. In the BS1 scenario, the first 67 UE positions has the LOS conditions. Therefore, the presence of LOS ray makes considerable difference in the power between the LOS ray and the NLOS ray. However, the FULLRT model shows slightly higher spread values and reaches the peak at some UE positions. This can be explained by comparing to Figures 32, 33, 34. The ASA in the NLOS UE positions are significantly high in the METIS and the HYBRID model. Since there are multiple AOAs, and the power of the NLOS rays varies to each ray, the spread value is high. The power of the NLOS rays is concentrated in one direction and has a medium value. It resulted in the moderate value of the spread. The ASA in the BS3 scenario is analogous to the BS1 scenario. The explanation to the lower spread values of the NLOS UE location in the BS2 scenario is that the arrival angle in the NLOS UE location is centred around -100°. Therefore, the power of rays is opulently distributed in the direction. Like in the case of ASA, ASD also can be related to AOD statistics in Figures 38, 39, and 40.

Secondly, the azimuth spread of departure is presented in Figures 47, 48, and 49.

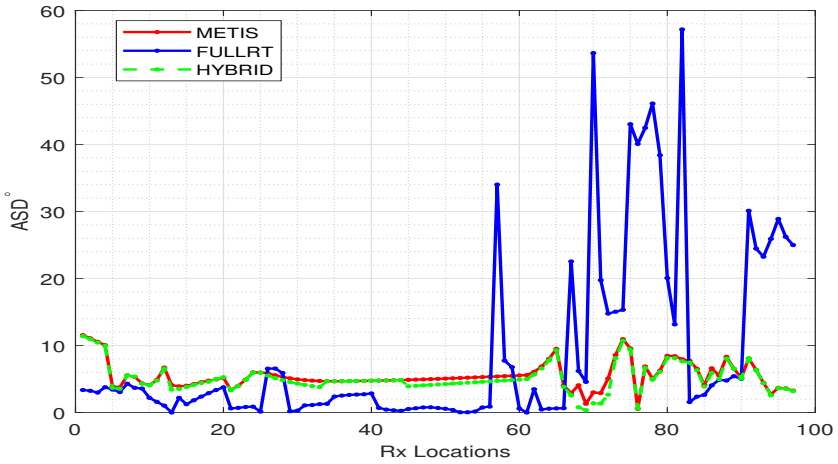

Figure 47. ASD in the BS1 scenario.

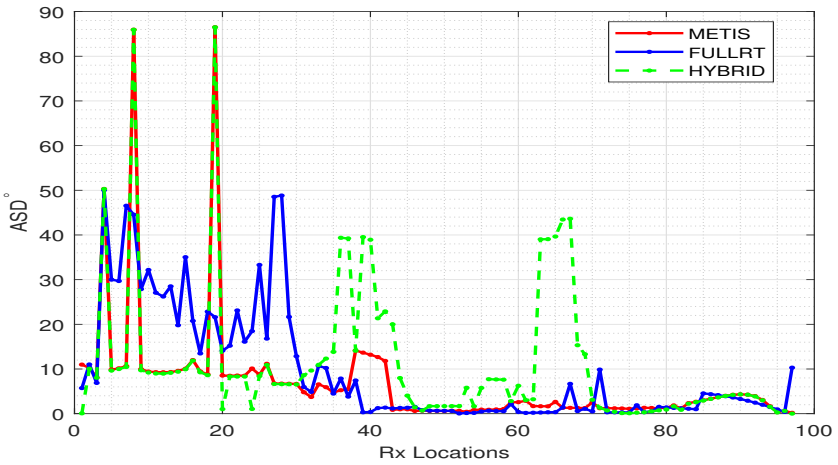

Figure 48. ASD in the BS2 scenario.

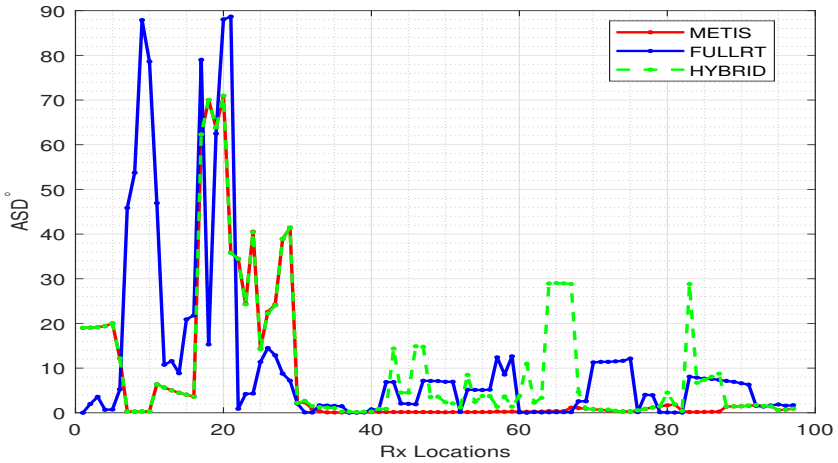

Figure 49. ASD in the BS3 scenario.

The spreads of the METIS model in the BS1 scenario varied between 4° and 10° in all UE positions. This behavior in NLOS is different to what is depicted in the NLOS ASA in the BS1 scenario. From the AOD it is seen in the NLOS departure direction is around 5°. It is evident for the lower spreads in the METIS model. The spread values of the FULLRT model can explained in the similar fashion in the ASA.

Thirdly, the comparison of the ESA in the BS1, BS2, and BS3 scenarios are given in Figures 50, 51 and 52.

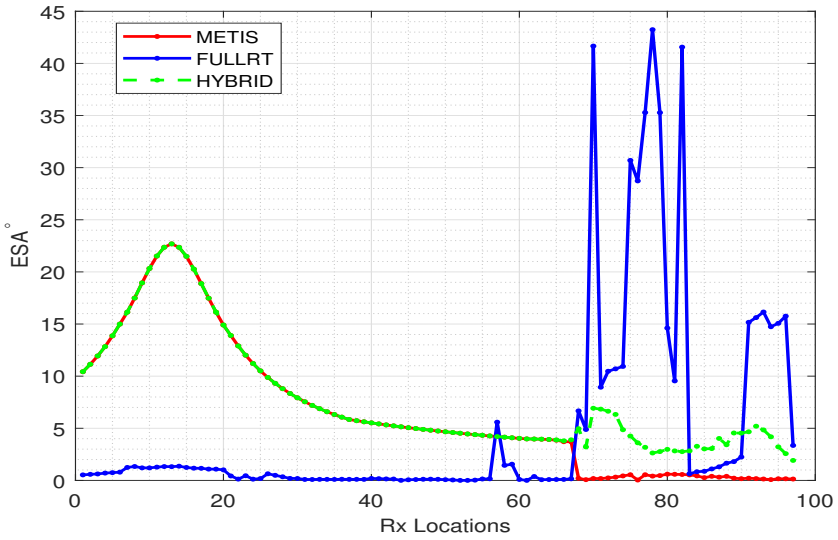

Figure 50. ESA in the BS1 scenario.

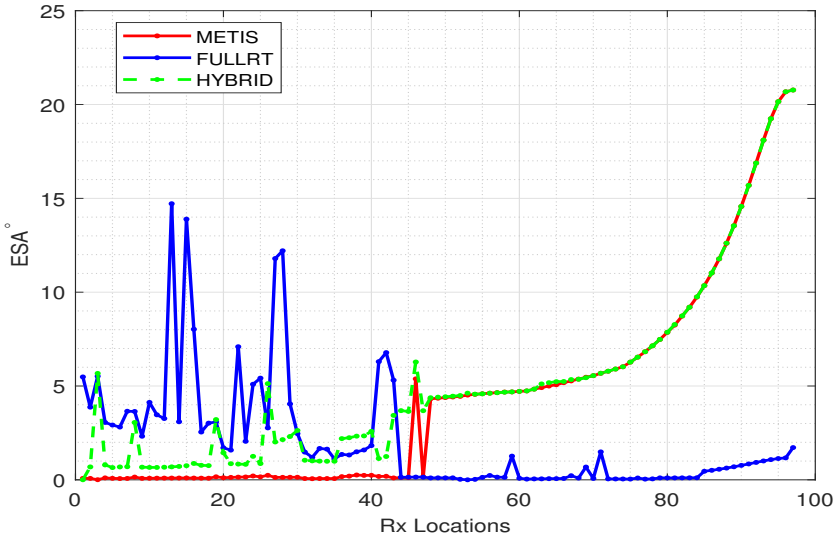

Figure 51. ESA in the BS2 scenario.

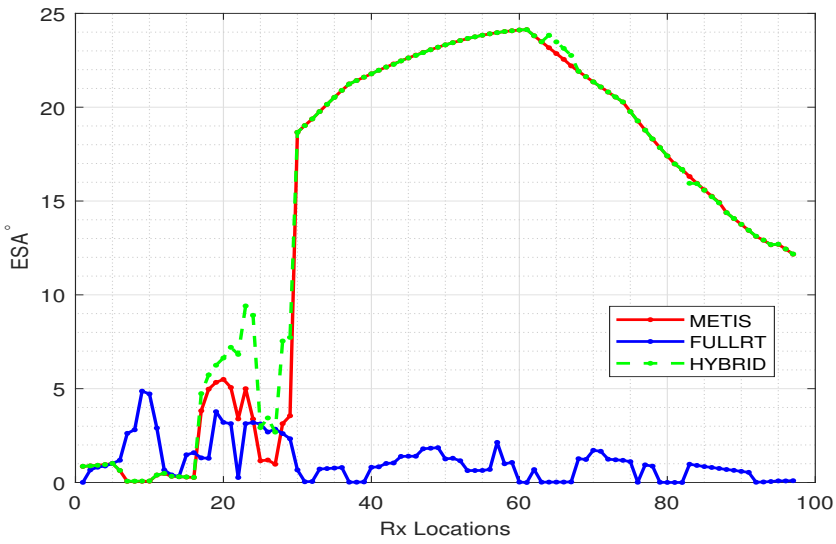

Figure 52. ESA in the BS3 scenario.

The ESA in the BS1 scenario, the METIS model starts with $10°$ and reaches a peak at the 16^{th} UE position and gradually decreases by reaching $2°$ at the 97^{th} UE position. Like in azimuth spreads the HYBRID and the METIS model have shown similar trends. The elevation angle of arrival in the BS1 scenario is centered around $0°$ but the spreads values are moderately high in LOS UE positions. Even though the rays arrive at almost the same angle at the elevation domain, only one ray is observed with higher power which has a different elevation angle.

The PAS figures are presented in order to analyze the critical spread values. Figure 53 is presented to illustrate the situation at the 13^{th} UE position where all rays except the LOS ray comes in same elevation angle but the LOS ray arrive at around $100°$ causing the dispersion.

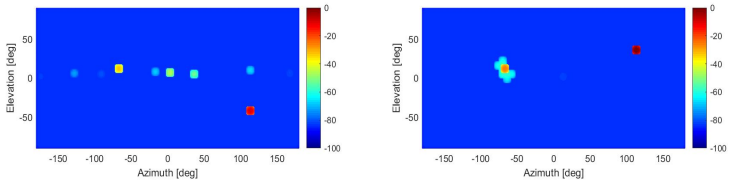

(a) (b)

Figure 53. Power angular spectrum seen by the UE at the 13^{th} UE position : (a) METIS, (b) FULLRT.

Figure 53 shows that the LOS ray has different elevation angle than NLOS rays in both METIS and the FULLRT model. Similarly, for the BS2 and the BS3 scenarios, the UE positions 50 and 40 PAS figures given to verify this explanation.

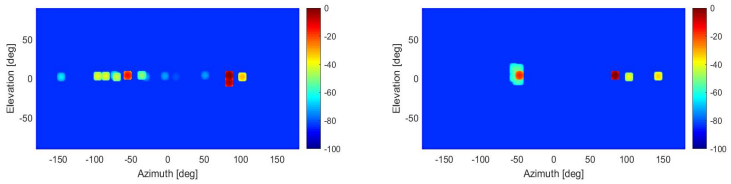

(a) (b)

Figure 54. Power angular spectrum seen by the UE at the 50^{th} UE position : (a) METIS (b) FULLRT.

Figure 54 illustrate the PAS at the UE location 50. It is seen in that in the elevation domain the rays are aligned in the same direction in the METIS model and there are small differences in the EOA in the FULLRT model. Next, the PAS at the UE position 40 is presented for the BS3 scenario.

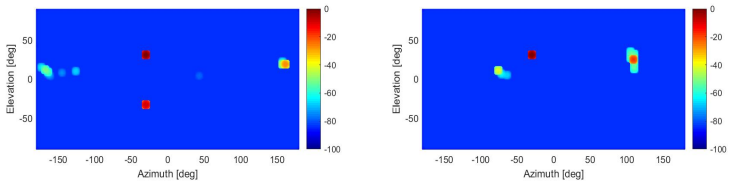

(a) (b)

Figure 55. Power angular spectrum seen by UE at 40^{th} UE position : (a) METIS (b) FULLRT.

The elevation spread rises sharply at the UE position 40. The reason is illustrated in Figure 55, where the rays with higher power with various EOA are seen in elevation axis. Finally we present the ESD in BS1, BS2, and BS3 scenarios in Figures 56, 57 and 58 .

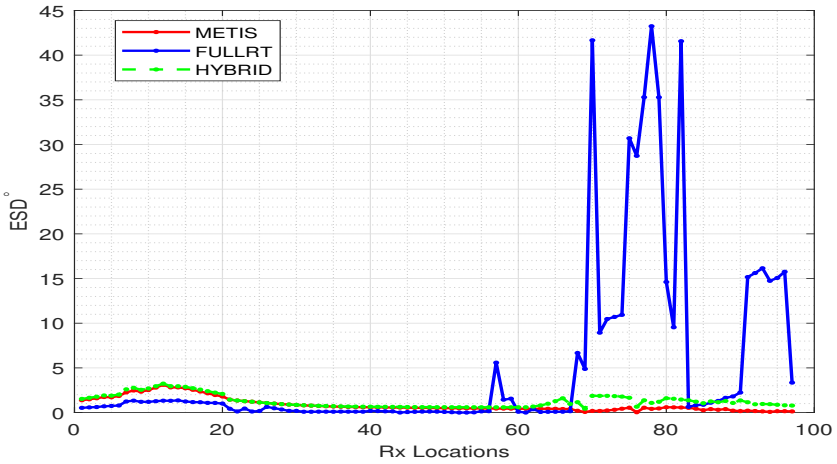

Figure 56. ESD in the BS1 scenario.

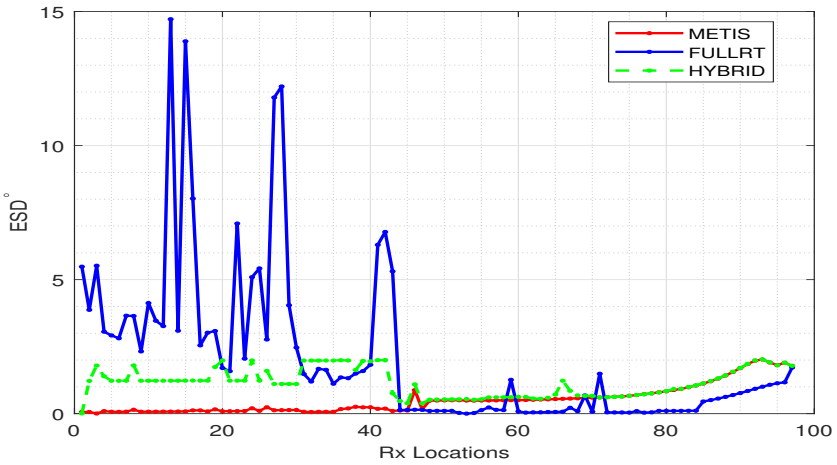

Figure 57. ESD in the BS2 scenario.

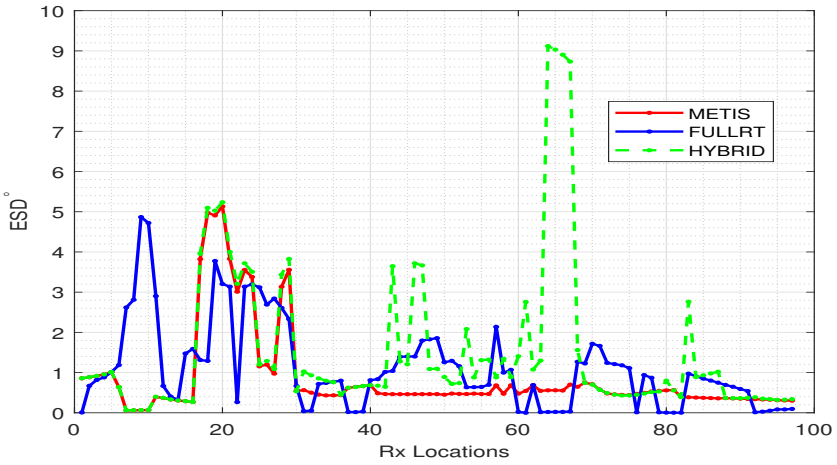

Figure 58. ESD in the BS3 scenario.

The elevation spreads in the BS1 and the BS2 scenarios for the METIS and the FULLRT models are less than $5°$. By referring to the EOD in Figures 41 and 42, it is evident almost every ray comes in the same direction in both the LOS and the NLOS UE positions and then the dispersion is reduced. But in the FULLRT models, there are higher probabilities seen for two angles which caused the higher spread values in the NLOS UE positions.

5.2.8 Delay spread

The RMS delay spread comparison in the BS1, BS2, and BS3 scenarios is presented for the METIS and the FULLRT model in Figures 59, 60, and 61. First we analyze the RMS DS in the BS1 scenario.

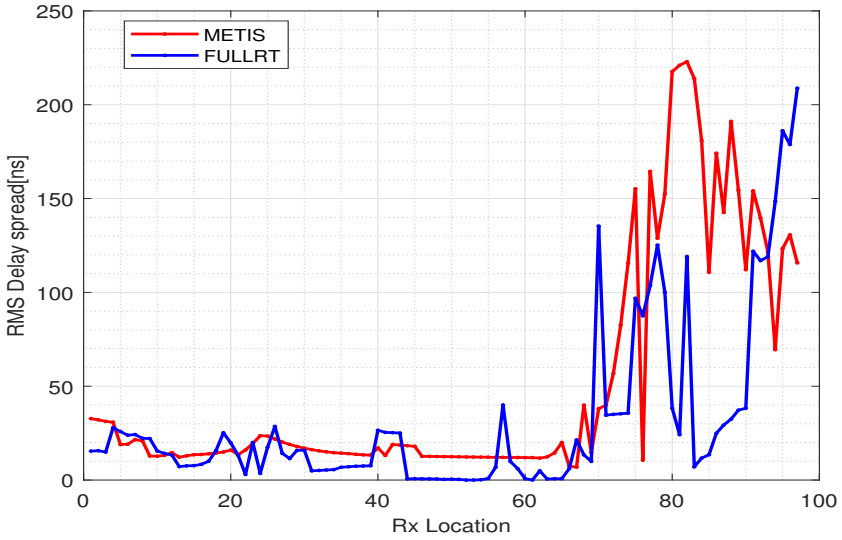

Figure 59. Delay spread comparison in the BS1 scenario.

In the BS1 scenario, DS values of both the FULLRT and the METIS model shows spread values less than 40 ns in the LOS UE positions. After the 67^{th} UE position, the DS values change dramatically. The DS in the METIS model fluctuates with higher values than the FULLRT model. Next, we present the RMS DS in the BS2 scenario in Figure 60.

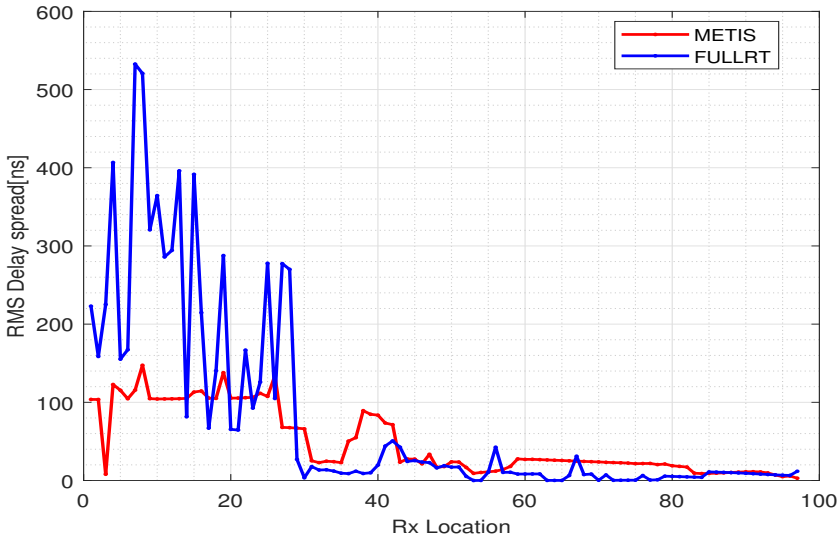

Figure 60. Delay spread comparison in the BS2 scenario.

Looking at the SP values in the BS2 scenario, the LOS UE positions have small spread values. But in the NLOS UE positions, the SP of the METIS model as unanticipated. By comparing the BS1 and the BS2 scenarios, it can be said that delay spread values in the NLOS locations are not necessarily the same. The delays are mainly determined by the deterministic feature of the environment. Lastly, we present the RMS DS analysis in the BS3 scenario in Figure 61.

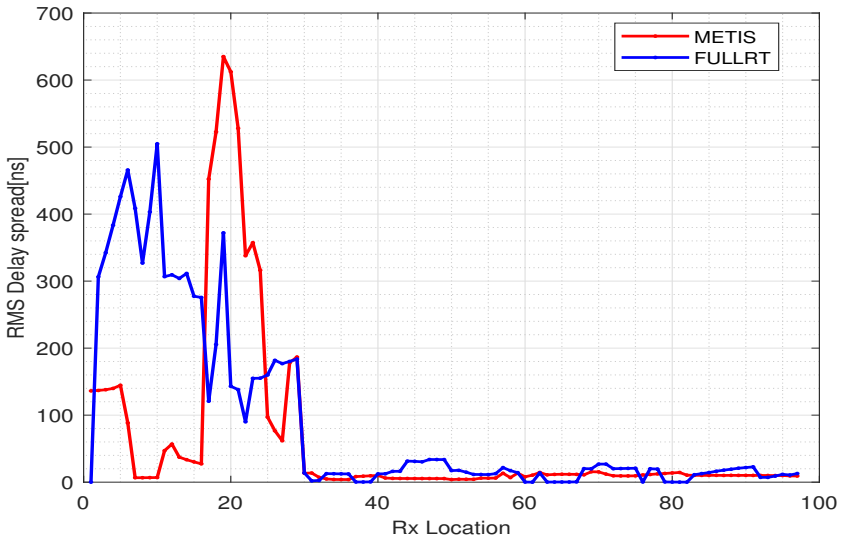

(a)

Figure 61. Delay spread comparison in the BS3 scenario.

Delay spreads values in the BS3 scenario show the known trend that the lower spread values in the LOS conditions and the higher spread values in the NLOS conditions. In three scenario, the most important finding is that, there is significant similarities between the two model where the LOS condition exists. It is indeed because of the

existences of the LOS ray that contributes to the shortest delay in the specific UE location.

5.2.9 Cross-polarization ratios

In this section, the cross-polarization ratios in the BS1, BS2, and BS3 scenario are discussed. This calculation was carried out by considering only the NLOS rays in each locations. Firstly, we present the XPRh results in Figures 62, 63, and 64.

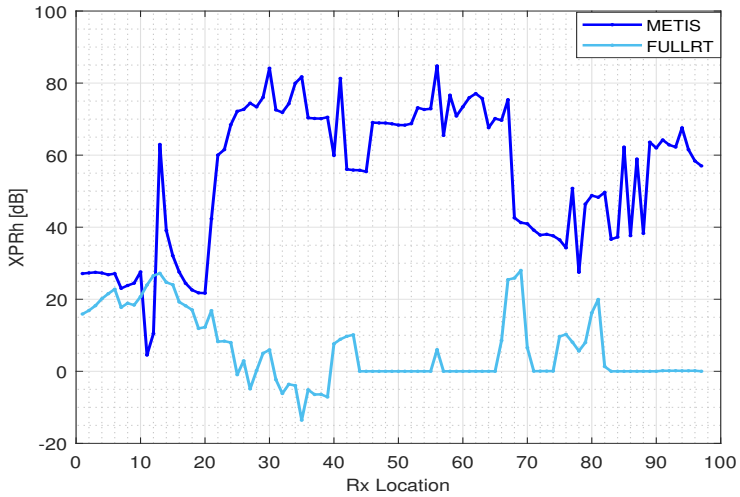

Figure 62. XPRh comparison of the METIS map-based model and the FULLRT model in the BS1 scenario.

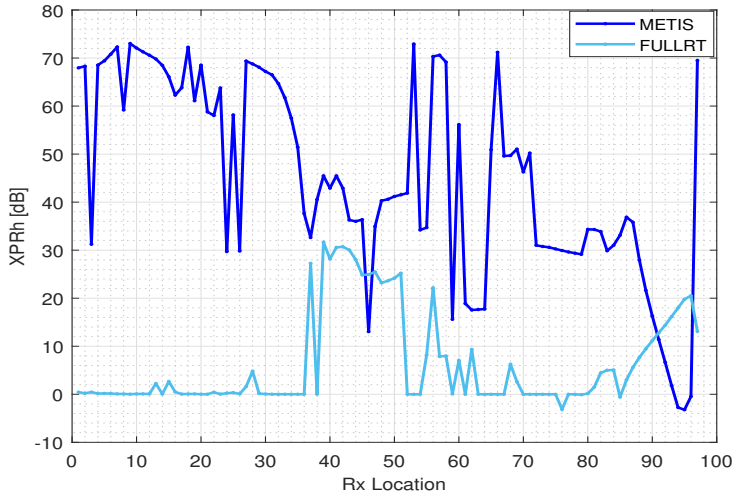

Figure 63. XPRh comparison of the METIS map-based model and the FULLRT model in the BS2 scenario.

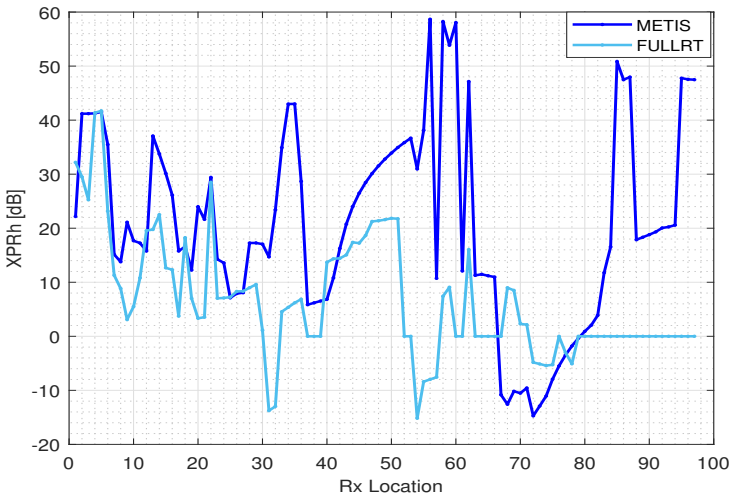

Figure 64. XPRh comparison of the METIS map-based model and the FULLRT model in the BS3 scenario.

In the BS1 and BS2 scenarios, the XPR_h of the FULLRT model is nearly 0 dB in majority of the UE positions. But in the METIS models it is above 20 dB in almost every UE positions. The power received at the orthogonal direction is comparatively low which has increased the ratio. Therefore, it seems that the power at the vertical polarization has been reduced dramatically in the rays modelled by the FULLRT. However, this observation is totally different in the BS3 scenario. In the first 31 UE positions and the UE positions from the $55th$ to the $60th$, similar trend is seen but in the other positions both models have shown contradicting results. Secondly, we present the XPRv results in the BS1, BS2, and BS3 scenarios in Figures 65, 66, and 67.

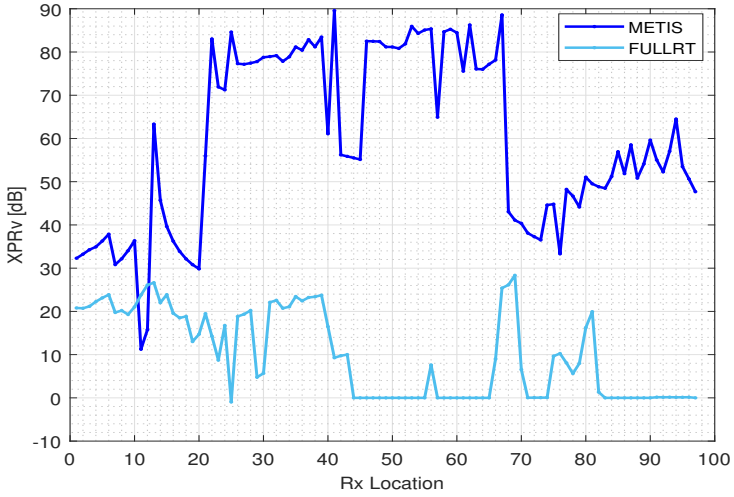

Figure 65. XPRv comparison of the METIS map-based model and the FULLRT model in the BS1 scenario.

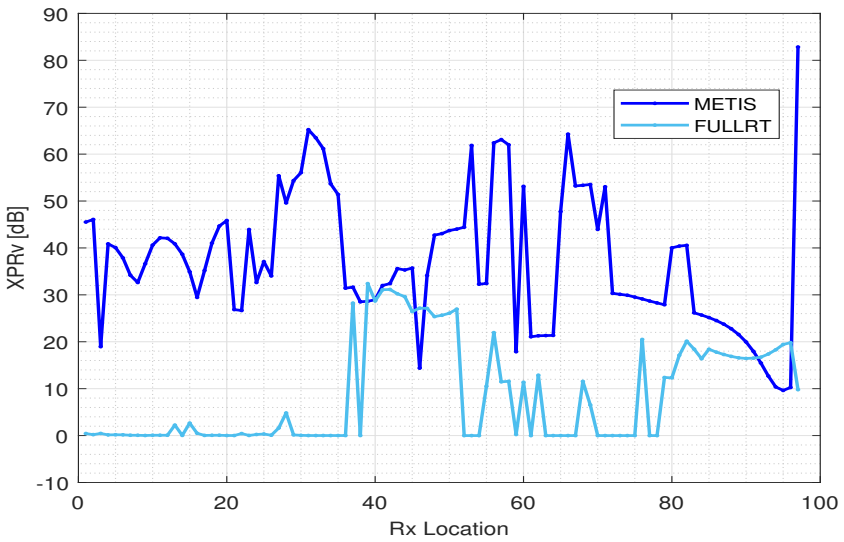

Figure 66. XPRv comparison of the METIS map-based model and the FULLRT model in the BS2 scenario.

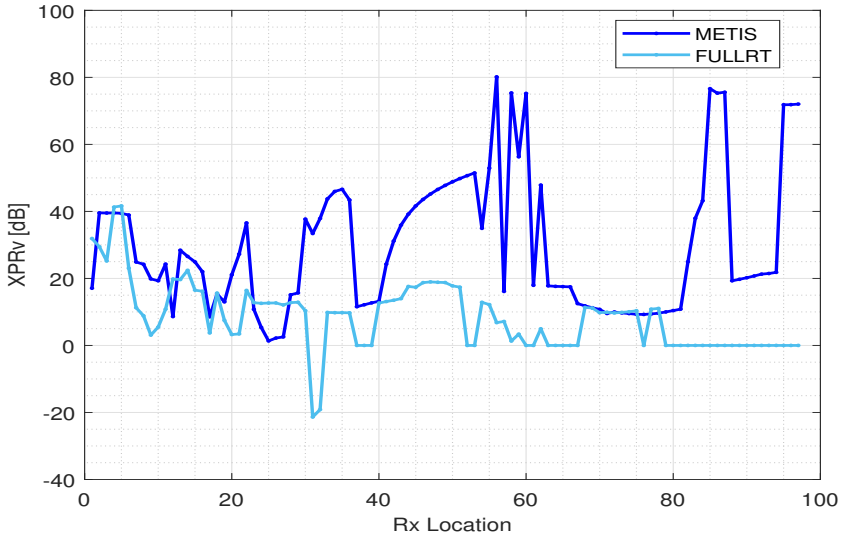

Figure 67. XPRv comparison of the METIS map-based model and the FULLRT model in the BS3 scenario.

In BS1 scenario, from the 45^{th} to $97th$ positions, the XPR_h and the XPR_v is same for the FULLRT model. It is difficult to explain the reason for discrepancies in the results but it might be related to the differences in the ray types and the relative permittivity of the building material. It is also noteworthy to mention that in the ray, which has multiple propagation mechanisms combined together, polarization of the ray is dramatically affected.

Next, we present the mean and standard deviation of the performance metrics in the Table 6. The mean and the standard deviation of the k-factor in the METIS and the HYBRID models are nearly equal. However, mean of the FULLRT model deviate

largely from other two models. The mean of the delay spreads and angle spreads are nearly equal in all three models.

Table 6: The mean and the standard deviation values of comparison parameters.

		Parameter	KF[dB]		DS[ns]		ASA[°]		ASD[°]		ESA[°]		ESD[°]	
			μ	σ	μ	σ	μ	σ	μ	σ	μ	σ	μ	σ
BS1	**METIS**	**LOS**	5.0291	1.7902	15.931	5.2674	5.0821	5.1679	5.3906	1.6778	9.4708	5.9813	1.1254	0.80414
		NLOS	NAN	NAN	126.51	61.05	25.038	13.011	5.7243	2.5174	0.3033	0.17266	0.3033	0.17265
	FULLRT	**LOS**	30.084	14.1	11.081	9.6429	5.5328	4.9641	2.7285	4.9718	0.53831	0.79305	0.53831	0.79305
		NLOS	NAN	NAN	75.613	59.422	18.599	10.463	21.483	16.472	14.65	13.649	14.65	13.649
	HYBRID	**LOS**	5.0344	1.7895	13.177	7.1898	4.4104	5.5964	5.0591	1.7382	9.4782	5.9773	1.2812	0.82482
		NLOS	NAN	NAN	123.26	61.724	24.248	13.808	5.2325	2.797	4.0011	1.3617	1.2551	0.38177
BS2	**METIS**	**LOS**	4.7712	1.4226	17.299	7.1901	5.6308	6.7444	1.771	1.1502	8.3419	5.003	0.88691	0.50404
		NLOS	NAN	NAN	81.482	37.885	13.077	13.211	12.274	17.26	0.23549	0.76874	0.13347	0.12471
	FULLRT	**LOS**	28.965	12.988	9.1828	8.5753	7.6599	7.841	1.6661	2.1638	0.3413	0.43462	0.3413	0.43462
		NLOS	NAN	NAN	162.14	150.29	30.697	20.977	19.269	14.392	4.2285	3.3882	4.2285	3.3882
	HYBRID	**LOS**	4.5135	1.7228	13.396	16.545	10.467	12.153	6.9055	11.889	0.93956	4.9898	0.93956	0.48082
		NLOS	NAN	NAN	86.768	47.973	19.662	24.219	15.823	18.671	1.7627	1.4319	1.3924	0.49223
BS3	**METIS**	**LOS**	11.033	8.1939	19.844	32.51	2.9885	2.0477	2.1379	4.6937	16.21	8.3737	0.48414	0.17979
		NLOS	NAN	NAN	335.56	203.83	51.842	17.853	41.837	19.12	3.5755	1.6225	3.2791	1.4132
	FULLRT	**LOS**	29.822	16.295	13.496	9.693	7.2931	6.7698	4.0989	3.9857	0.70827	0.58379	0.70827	0.58379
		NLOS	NAN	NAN	262.56	123.61	39.527	22.83	27.476	31.144	2.0639	1.3429	2.0639	1.3429
	HYBRID	**LOS**	10.85	8.2866	25.803	35.118	5.6814	6.6258	5.6062	7.7894	16.235	8.395	1.2511	1.8778
		NLOS	NAN	NAN	331.68	195.61	51.735	17.907	41.763	19.184	6.1562	2.1679	3.4306	1.4298

6 DISCUSSION

In this thesis, two deterministic channel models, namely the full tracing based model and the simplified map-based model are discussed and supported with the hybrid channel modelling method. This thesis work is focused in processing the map so that it can be used with the current METIS map based channel modelling tool and building comparison metrics. Some implementation principles are taken from the hybrid modelling approach to get the propagation channel parameters from the METIS map-based model. Initially, it was decided to compare the radio channel characteristics but due to the time factor, it was then limited to the propagation channel characteristics. The differences in the results of the LOS and the NLOS UE positions reveals the missmatches caused when simplifying the map.

The comparison of the number of paths is carried out to observe the strong paths as a percentage of the total paths. The number of paths does not necessarily mean the capability of the modelling tool to discover paths. All paths were gathered from the three modelling tools and the HYBRID model result is skipped due to the fact that, it is not meaningful to compare it with the other two models because of creating the 20 random rays on top of the cluster. In the UMi scenario, the LOS UE positions in the METIS model has higher number of rays within DR than the FULLRT model. This is because of that fact that the power of NLOS rays are strong in the METIS model. However, in the NLOS UE positions this situation is changed and higher number of rays within DR in the FULLRT model is noted. It is important to mention that in the NLOS position, DR is calculated based on the power of the strongest ray in that specific UE position. Though the power of the NLOS rays in the FULLRT models is weak, the low difference between the power is making the higher number within DR. The higher number within the DR in the LOS UE positions makes more reasonable than in the NLOS UE positions as it is an indication of good rays in that specific UE location.

The path loss comparison results show a similar trend in the LOS conditions and have a 50 dB different in the NLOS UE positions in the BS1 and the BS2 scenarios. This difference is no surprise when considering the fact that the rays in the real environment will have multiple propagation mechanisms combined together. However, the NLOS positions in the BS3, there is only 15 dB higher loss shown in the METIS model. This reveals that if the NLOS rays are modelled accurate enough then the results between all three models will tend to behave close enough. The path loss to FSPL comparison illustrates the multipath gain and losses from the METIS and the FULLRT model. This gain is calculated by taking the difference between FSPL and the total loss. The loss is high in all three BSs in the NLOS UE positions in the METIS model.

The power delay profile comparison is presented to observe the variation of the delays and the power along the UE positions. Both models have shown the inconsistent power with delays. There are rays with higher delays with considerable higher power compared to the middle area of PDP, which reveals the higher delay spread.

K-factor comparison had a dramatic difference between the METIS and the FULLRT model. It is obvious that if the powers of the NLOS rays are much lower than the power of the LOS ray, consequently the *KF* value will be large. The SD of the METIS model is very small. But the FULLRT model has 14.1 dB, 12.988 dB, 16.295 dB standard deviation for the scenarios BS1, BS2, and BS3, respectively. This also indicates that

in order to get a realistic *KF*, the precise modelling of the NLOS rays is essential. Furthermore, the ground reflected rays were not seen among the NLOS rays.

In the angular statistics comparison, azimuth angle reveals multipath richness of the environment as there are various azimuth angles observed. There are similarities in the elevation angle comparisons. However, that shift in the angle reveals there is a possibility of human error in the calculation of the height of the first and the last interaction points when simplifying the map. Angle spreads are influenced by the LOS ray power and the spread values in the LOS UE positions are observed to be near to 0°.

The mean and average of the delay spread value in the METIS model is higher than in the FULLRT model. In the NLOS UE locations, significantly higher spread values are exhibited in the METIS model and considerably higher spread values are seen in the FULLRT model. The discrepancies in the delay spread are also due to the rays with the longer delays, which is a result of the rays having three-order interaction and multiple propagation mechanisms. The delay spreads and angle spreads are strongly correlated and they are affected by the LOS path to a greater extent. The results of the cross polarization ratios are hard to interpret or put a reason for the dissimilarities. In contrast, most of the discrepancies in all results are caused due to variations in the LOS and the NLOS UE conditions and dissimilarities in features.

7 CONCLUSION

The main goal of this thesis was to investigate and compare the propagation channel characteristics from the three channel models: 1) the simplified map based model, 2) the full ray tracing based model, and 3) the hybrid channel model which is based on the map based implementation. The results of the LOS and the NLOS UE position analyses have shown that, the simplifying causes mismatches in the propagation conditions in a specific UE location. It was also found that in the UE positions where this kind of mismatch has caused dramatic discrepancies in the results. Next, the number of rays within the 60 dB DR is analyzed.

The finding from these results provides how many stronger NLOS rays with respect to the LOS ray are modelled. In the NLOS UE location it portrays the portion of good rays among the NLOS rays. The number of rays and the number of rays within DR was high in the METIS model than the FULLRT model. The results of the K-factor suggest that to get similar *KF*, the NLOS rays should be modelled accurately. Statistics of angle describe how well the arrival and the departure angles of rays are distributed in the azimuth and the elevation domains. Three models, present the rays that are well distributed in the azimuth domain. However, the difference in the elevation angle probabilities could be due to the error while processing the simplifying map. The spreads of angle in the LOS UE positions are as anticipated. It is hard to come to the conclusion about the spreads in the NLOS UE locations due to the differences in the modelled NLOS rays.

Next, we analyzed the delay spread. The delay spreads in the NLOS UE positions had significant differences in the values. The reason is same as in the angle spreads. It is unfortunate that the cross polarization comparison result does not warrant any true conclusion based on these results. Notwithstanding these unanticipated results, it offers some insight into how these polarization ratios can be affected in the high dense urban environment.

Finally, a number of important limitations need to be acknowledged. The main challenge of this comparison work was the paucity of the good data. The chosen environment itself is a high dense urban environment. The highest of the building is 60 m. The number of the UE positions are 97 and the METIS map-based model and the hybrid model takes significantly larger time to run the simulation. Furthermore, it needs to be noted that in the simplified concept the material related parameters, such as relative permittivity, are assumed to be same for all buildings.

Despite of these limitations, differences and challenges, the results in this thesis reveal some practices to be considered when comparing the ray tracing based channel models. It is essential for the ray tracing based model to determine the propagation condition correctly and the models should have identical propagation condition in each UE positions. When comparing the ray tracing based models at least the main features, such as supported propagation mechanisms, order of interaction, and the map used in the models should be identical. In the results, there should be a sufficient number of good rays in each UE position in order to get meaningful results. It would benefit to a ray-tracing tool to model the rays with multiple propagation mechanism, so that the NLOS rays are realistic. As the future study, it is decided to embed the antenna and investigate the radio channel characteristics of the three models.

8 REFERENCES

[1] Rappaport T.S., Xing Y., MacCartney Jr G.R., Molisch A.F., Mellios E. & Zhang J. (2017) Overview of millimeter wave communications for fifth-generation (5G) wireless networks-with a focus on propagation models. arXiv preprint arXiv:1708.02557 .

[2] Ghosh A. et al. (2015) 5G channel model for bands up to 100 GHz. 5GCM white paper .

[3] 3GPP (2011) 3^{rd} generation partnership project; technical specification group radio access network; evolved universal terrestrial radio access (E-UTRA); user equipment (UE) conformance specification radio transmission and reception .

[4] R1-160823 (2018) "5G channel model requirements vs. modelling approaches". Technical specification (TS), 3^{rd} Generation Partnership Project (3GPP).

[5] Rappaport T.S., Sun S. & Shafi M. (2017) Investigation and comparison of 3GPP and nyusim channel models for 5G wireless communications. In: 2017 IEEE 86th Vehicular Technology Conference (VTC-Fall), pp. 1–5.

[6] Hekkala A., Kyösti P., Dou J., Tian L., Zhang N., Zhang W. & Gao B. (2017) Map-based channel model for 5G wireless communications. In: 2017 XXXIInd General Assembly and Scientific Symposium of the International Union of Radio Science (URSI GASS), pp. 1–4.

[7] R1-161619 (2018) "map-based hybrid model". Technical specification (TS), 3^{rd} Generation Partnership Project (3GPP).

[8] Salous S. (2013) Radio propagation measurement and channel modelling. John Wiley & Sons.

[9] Nurmela V., Karttunen A., Roivainen A., Raschkowski L., Hovinen V., Omaki N., Kusume K., Hekkala A., Weiler R. et al. (2015) Deliverable d1. 4 metis channel models. In: Proc. Mobile Wireless Commun. Enablers Inf. Soc.(METIS), p. 1.

[10] De la Roche G., Alayón-Glazunov A. & Allen B. (2012) LTE-advanced and next generation wireless networks: channel modelling and propagation. John Wiley & Sons.

[11] Keller J.B. (1962) Geometrical theory of diffraction. JOSA 52, pp. 116–130.

[12] Berg J.. (1995) A recursive method for street microcell path loss calculations. In: Proceedings of 6th International Symposium on Personal, Indoor and Mobile Radio Communications, vol. 1, vol. 1, pp. 140–143 vol.1.

[13] Liebenow U. & Kuhlmann P. (1994) Theoretical investigations and wideband measurements on wave propagation in hilly terrain. In: Proceedings of IEEE Vehicular Technology Conference (VTC), IEEE, pp. 1803–1806.

[14] Degli-Esposti V. (2001) A diffuse scattering model for urban propagation prediction. IEEE Transactions on Antennas and Propagation 49, pp. 1111–1113.

[15] METIS2020 D. (2015) D1. 4 v3. METIS channel model .

[16] Katalinić Mucalo A., Zentner R. & Mataga N. (2012) Benefits and challenges of deterministic reference channel models. Automatika: časopis za automatiku, mjerenje, elektroniku, računarstvo i komunikacije 53, pp. 80–87.

[17] Mani F. (2012) Improved ray-tracing for advanced radio propagation channel modeling. PhD dissertation, PhD Thesis, ICTEAM, UCL Belgium.

[18] Yun Z. & Iskander M.F. (2015) Ray tracing for radio propagation modeling: Principles and applications. IEEE Access 3, pp. 1089–1100.

[19] He D., Ai B., Guan K., Wang L., Zhong Z. & Kürner T. (2018) The design and applications of high-performance ray-tracing simulation platform for 5G and beyond wireless communications: A tutorial. IEEE Communications Surveys Tutorials , pp. 1–1.

[20] Kaya A.O., Trappe W., Greenstein L.J. & Chizhik D. (2012) Predicting MIMOperformance in urban microcells using ray tracing to characterize the channel. IEEE Transactions on Wireless Communications 11, pp. 2402–2411.

[21] Meinilä J., Kyösti P., Jämsä T. & Hentilä L. (2009) Winner ii channel models. Radio Technologies and Concepts for IMT-Advanced , pp. 39–92.

[22] R1-160620 (2018) "Details in hybrid channel modelling". Technical specification (TS), 3^{rd} Generation Partnership Project (3GPP).

[23] R1-161659 (2018) "Description of map–based hybrid model with simulation example". Technical specification (TS), 3^{rd} Generation Partnership Project (3GPP).

[24] 38.901 (2018) Study on channel model for frequencies from 0.5 to 100 GHz. Technical Specification (TS) Release 15, 3^{rd} Generation Partnership Project (3GPP).

[25] Kyösti P. (2018) Radio channel modelling for 5G telecommunication system evaluation and over the air testing. D.Sc dissertation, University of Oulu.

[26] Fitton M.P., Nix A.R. & Beach M.A. (1996) A comparison of rms delay spread and coherence bandwidth for characterisation of wideband channels. In: IEE Colloquium on Propagation Aspects of Future Mobile Systems (Digest No: 1996/220), pp. 9/1–9/6.

[27] Saunders S. & Aragón-Zavala A. (2007) Antennas and propagation for wireless communication systems. John Wiley & Sons.

[28] Meinilä J., Kyösti P. et al. (2010) D5. 3: Winner+ final channel models v1. 0. jun. 2010. Article (CrossRef Link) .

[29] Haneda K., Poutanen J., Liu L., Oestges C., Tufvesson F. & Vainikainen P. (2010) Comparison of delay and angular spreads between channel measurements and the COST2100 channel model. In: 2010 Loughborough Antennas Propagation Conference, pp. 477–480.

[30] 3GPP (2003) Circular angle spread. Teleconference, 3^{rd} Generation Partnership Project (3GPP).

[31] 3GPP (2018) Spatial channel model for Multiple Input Multiple Output (MIMO) simulations. Technical Specification (TS) 25.996, 3^{rd} Generation Partnership Project (3GPP). URL: `https://portal.3gpp.org/desktopmodules/Specifications/SpecificationDetails.aspx?specificationId=1382`, version 15.0.0.

[32] Jiang L., Thiele L. & Jungnickel V. (2007) On the modelling of polarized MIMO channel. Proc. Europ. Wireless 2007, pp. 1–4.

[33] Mukherjee S., Das S.S., Chatterjee A. & Chatterjee S. (2017) Analytical calculation of rician k-factor for indoor wireless channel models. IEEE Access 5, pp. 19194–19212.

[34] Roivainen A. (2017) Three-dimensional geometry-based radio channel model : parameterization and validation at 10 GHz. D.Sc dissertation, University of Oulu.

[35] Friis H.T. (1946) A note on a simple transmission formula. proc. IRE 34, pp. 254–256.